



Available online at www.sciencedirect.com

ScienceDirect

Comput. Methods Appl. Mech. Engrg. 378 (2021) 113737

**Computer methods
in applied
mechanics and
engineering**

www.elsevier.com/locate/cma

RI-IGABEM for 2D viscoelastic problems and its application to solid propellant grains

Deyong Sun, Rui Dai, Xiangyang Liu*, Yunsheng Zhan, Chunying Dong*

School of Aerospace Engineering, Beijing Institute of Technology, Beijing 100081, China

Received 6 January 2021; received in revised form 11 February 2021; accepted 15 February 2021

Available online 5 March 2021

Abstract

The isogeometric boundary element method (IGABEM) has a broad application prospect due to its exact geometric representation, excellent field approximation and only boundary discretization property. In this paper, IGABEM based on radial integration method (RI-IGABEM) is used for viscoelastic analysis of solid propellant grain. The memory stress, as the initial stress, leads to the boundary-domain integral equations and thus eliminates the only boundary discretization advantage of boundary element method (BEM). The radial integration method (RIM) is applied to transform the domain integral into an equivalent boundary integral by means of the applied points. The usage of RIM makes it possible to only store the strains on the applied points. Meanwhile, Prony-series is used to discretize the general integrals and to store the two most recent time-step strains rather than the time-step strains of the entire process. The combination between RIM and Prony-series will help reduce the storage space and computational time. In addition, by using the fundamental solutions for linear elastic problems and the regularized technologies, the singular integrals can be solved through the previous methods, such as the Telles scheme and element sub-division method. In order to validate the accuracy and robustness of RI-IGABEM in viscoelastic analysis, the influence of the number and position of applied points as well as the time interval on viscoelastic analysis is discussed through comparing with cell discretization methods. A set of numerical examples demonstrates the ability of the scheme to simulate the viscoelastic problems.

© 2021 Elsevier B.V. All rights reserved.

Keywords: Isogeometric boundary element method; Viscoelastic analysis; Radial integration method; Prony series; Solid propellant grain

1. Introduction

In the process of casting, curing, cooling and long-term storage of solid propellant, due to the influence of processing technology, residual stress and environment, defects such as inclusions, holes, debonding and cracks often occur, which will affect the quality and life of solid propellant. It is essential to pay more attention on the accurate stress-strain field around the defects during the process of structural integrity assessment [1,2]. Finite element method (FEM) [3] and BEM [4] are two standard numerical tools to obtain the stress-strain fields, especially in linear elastic problems [5]. However, it is very difficult and time consuming to simulate the stress-strain field around small defects by FEM.

* Corresponding authors.

E-mail addresses: liuxy@bit.edu.cn (X. Liu), cydong@bit.edu.cn (C. Dong).

It is well known that the semi-analytical property of BEM makes it a more accurate and powerful numerical simulation method. In engineering simulation, there are other appealing features, such as using only boundary discretization instead of domain discretization which occupies 80% of the total linear elastic solving time [6], reducing the dimensions by one, and automatically satisfying the boundary conditions at infinity. Meanwhile, the only boundary discretization feature is strengthened by the concept of the isogeometric analysis (IGA), in which the CAD model can be converted into analysis model directly through knot-insertion, degree-elevation or by k -refinement (high-degree and maximal smoothness). Due to the exactly defined geometry from CAD, unnecessary geometric refinement will decrease the simulation efficiency. The Geometry Independent Field approximaTion (GIFT) [7,8] gives another mesh refinement strategy to improve efficiency and keep accuracy simultaneously. The combination between IGA and BEM called IGABEM has been successfully applied to solve many practical problems such as potential problem [9,10], elastic problem [11], acoustics problems [12,13], heat conduction [14], crack propagation [15], Helmholtz problems [16] and shape optimization [17,18]. However, due to tensor product form of NURBS, NURBS-based IGABEM has two critical drawbacks: (1) the complex geometry cannot be described by one NURBS patch; (2) it is difficult to achieve local refinement on the NURBS patches. Several methods [19–25] have been proposed to alleviate those difficulties faced by initial IGA. More details about IGA can be found in review papers [26,27]. Meanwhile, the drawback about the non-symmetric and dense matrices in BEM is not avoidable in IGABEM, which restricts the efficiency of solving large-scale problems. In order to improve the computational efficiency of BEM, various accelerated algorithms have been adopted, such as Fast Multipole Method (FMM) [28], the wideband FMM [29], Adaptive Cross Approximation (ACA) [30], the fast wavelet transforms [31], and the precorrected fast Fourier transformation (FFT) [32].

The key points to solving nonlinear problems, such as plastic problem [33–35] and elastodynamic problem [36] by BEM are domain integrals and their singularities. The RIM has successfully combined with IGABEM (RI-IGABEM) to deal with domain integrals in transient heat conduction problems [14]. For singularities, Telles [37] proposed a self-adaptive algorithm to improve the accuracy of Gaussian quadrature approach within the near-singularity range. The rigid body displacement method [38] was developed to eliminate the singularity on collocation points corresponding to coefficient matrices. In this method, the elements in coefficient matrices must be calculated accurately except for the diagonal elements. The regularized form of boundary integral equation [39–41] can avoid calculation of strongly singular integrals and jump terms, but this method can only reduce the singular order by one in 2D, and cannot completely avoid the hyper singularity. This method combines RIM to reduce the singular order in domain integrals. Meanwhile, many methods have been introduced to solve various singularities, including new Gaussian quadrature approach [42], the local regularization method [43,44], transformation method [37,45,46], finite-part integral method [47], etc. The power series expansion method presented by Gao [48] was used to compute the singular integrals, and its applications can be found in [49].

To the authors' knowledge, viscoelastic analysis using the RI-IGABEM algorithm has not yet occurred. In this paper, the RI-IGABEM is extended to two-dimensional viscoelastic materials to simulate the creep, relaxation and recovery behaviors of viscoelastic materials. The paper is organized as follows. In Section 2, the basic properties of NURBS and IGABEM for linear elastic problems are briefly introduced. Section 3 derives the regularized domain-boundary integral equations for viscoelastic problems and their isogeometric implementation. Section 4 illustrates relevant iteration process for time-dependent viscoelastic analysis. In Section 5, some numerical examples about viscoelastic problems are given to demonstrate the robustness of numerical algorithms and related factors. Section 6 shows some conclusions and future work.

2. BEM and IGABEM

2.1. Boundary integral equation for linear elastic problems

The BEM is a powerful tool for solving a series of engineering problems, in which the partial differential equation (PDE) can be reformulated as boundary integral equation by Green's function, and the boundary integral equation only contains the unknown fields on the boundary. In the present work, we focus on the application of BEM for 2D plane strain problem. Consider an arbitrary domain Ω whose boundary $\Gamma \equiv \partial\Omega$, the discrete form of displacement boundary integral equation (DBIE) for linear elastic problems is formulated as [50]

$$\mathbf{C}(\mathbf{x})\mathbf{u}(\mathbf{x}) = \int_{\Gamma} \mathbf{U}(\mathbf{x}, \mathbf{y})\mathbf{t}(\mathbf{y})dS - \int_{\Gamma} \mathbf{T}(\mathbf{x}, \mathbf{y})\mathbf{u}(\mathbf{y})dS + \int_{\Omega} \mathbf{U}(\mathbf{x}, \mathbf{y})\mathbf{b}(\mathbf{y})d\Omega \quad (1)$$

where Γ is the boundary of domain, \mathbf{x} and \mathbf{y} are the source point and field point on the boundary, respectively. $\mathbf{C}(\mathbf{x})$ is the jump term that arises from the strongly singular nature of the traction kernel. \mathbf{u} , \mathbf{t} and \mathbf{b} mean the displacement, traction and body force vectors, respectively. $\mathbf{U}(\mathbf{x}, \mathbf{y})$ and $\mathbf{T}(\mathbf{x}, \mathbf{y})$ are the fundamental solutions of linear elastic problems.

The displacement and traction fundamental solutions in 2D plane strain problem for isotropic materials are given as

$$U_{ij}(\mathbf{x}, \mathbf{y}) = \frac{1}{8\pi\mu(1-v)}[(3-4v)\ln\frac{1}{r}\delta_{ij} + r_{,i}r_{,j}] \quad (2)$$

$$T_{ij}(\mathbf{x}, \mathbf{y}) = -\frac{1}{4\pi(1-v)r}[r_{,n}((1-2v)\delta_{ij} + 2r_{,i}r_{,j}) + (1-2v)(n_jr_{,i} - n_ir_{,j})] \quad (3)$$

where n_i is the unit normal component on x_i direction, and $r = |\mathbf{x} - \mathbf{y}|$ is the distance between source point and field point, and $r_{,i} = \frac{\partial r}{\partial x_i}$ is the partial derivative in i th direction. v is Poisson's ratio, μ is the shear modulus, and δ_{ij} is the Kronecker delta. Note that the kernel function U is weak singular kernel with $O(\ln(\frac{1}{r}))$, and the kernel function T is strong singular kernel with $O(\frac{1}{r})$ in 2D problems.

We can solve Eq. (1) under a set of boundary conditions

$$u(\mathbf{x}) = \bar{u}, \quad \mathbf{x} \in \Gamma_D \quad (4)$$

$$t(\mathbf{x}) = \bar{t}, \quad \mathbf{x} \in \Gamma_N \quad (5)$$

The known quantities \bar{u} and \bar{t} are prescribed displacements and tractions, respectively; Γ_D and Γ_N denote the Dirichlet and Neumann boundaries, respectively.

2.2. B-splines and NURBS

In the concept of IGA, physical and parametric spaces can be described by different splines simultaneously, such as NURBS, T-spline or PHT, which can help engineers eliminate the gap between CAD and CAD and skip time-consuming process, i.e. mesh regeneration. In this paper, the NURBS basis function is briefly introduced here for completeness, and more details can be found in reference [50].

A knot vector is a set of non-decreasing real number in the parametric space, which is the basis of NURBS, as shown below

$$\Xi = \{\xi_1, \xi_2, \dots, \xi_{n+p+1}\}, \quad \xi_a \in \mathbb{R} \quad (6)$$

where the subscript a denotes the knot index, p is the curve order, and n is the number of basis functions or control points. The half open interval $[\xi_i, \xi_{i+1})$ is called a knot span.

With the concept of a knot vector, the B-spline basis functions are defined using the Cox–de Boor recursion formula

$$N_{a,0} = \begin{cases} 1, & \text{if } \xi_a \leq \xi \leq \xi_{a+1}. \\ 0, & \text{otherwise.} \end{cases} \quad (7)$$

for $p = 0$, and

$$N_{a,p}(\xi) = \frac{\xi - \xi_a}{\xi_{a+p} - \xi_a} N_{a,p-1}(\xi) + \frac{\xi_{a+p+1} - \xi}{\xi_{a+p+1} - \xi_{a+1}} N_{a+1,p-1}(\xi) \quad (8)$$

for $p = 1, 2, 3, \dots$

B-spline basis functions are C^∞ within elements and C^{p-m} on element boundary, where m is the number of knot repetitions (see Fig. 1). And B-spline basis functions possess several favorable properties such as local support, pointwise non-negativity, linear independence. As shown in Fig. 1, a whole B-spline curve can be defined by n basis functions in Eqs. (7) and (8) as well as control points $\mathbf{P}_a (a = 1, 2, \dots, n)$.

The B-spline curve can be constructed as a linear combination of B-spline basis functions and control points, i.e.

$$\mathbf{x}(\xi) = \sum_{i=1}^n N_{a,p}(\xi) \mathbf{P}_a \quad (9)$$

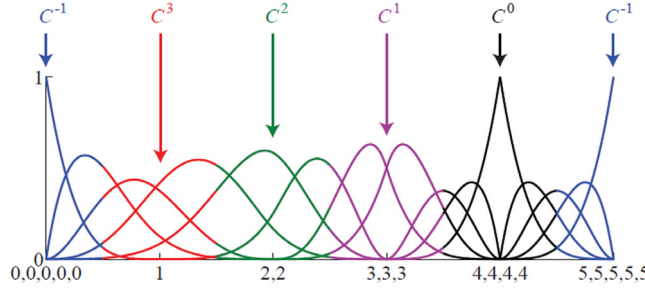


Fig. 1. NURBS basis functions.

where the coefficients \mathbf{P}_a denote the coordinates of control points, and $\mathbf{x} = (x, y, z)$ is the location of the physical space corresponding to the coordinate ξ in parametric space. NURBS are the extension of B-spline by assigning a positive weight ω_a to each basis function:

$$\mathbf{x}(\xi) = \sum_{a=1}^n R_{a,p}(\xi) \mathbf{P}_a \quad (10)$$

where $R_{a,p}$ are the NURBS basis functions, i.e.

$$R_{a,p}(\xi) = \frac{N_{a,p}(\xi) \omega_a}{W(\omega)} \quad (11)$$

with

$$W(\xi) = \sum_{a=1}^n N_{a,p}(\xi) \omega_a \quad (12)$$

At this point it is noticeable that the control points do not lie on the spline curve, which are the most important difference between IGABEM and traditional BEM.

2.3. IGABEM for linear elastic problem

Unlike traditional BEM, in the application of isogeometric analysis, the geometry and field variables are described by NURBS or other splines simultaneously. The displacement and traction vectors on the boundary are expressed using NURBS basis functions, i.e.

$$\mathbf{u}(\xi) = \sum_{A=1}^{N_A} R_A(\xi) \tilde{\mathbf{u}}_A \quad (13)$$

$$\mathbf{t}(\xi) = \sum_{A=1}^{N_A} R_A(\xi) \tilde{\mathbf{t}}_A \quad (14)$$

where $\tilde{\mathbf{u}}_A, \tilde{\mathbf{t}}_A$ are global displacement and traction parameters associated with control points by index A [32,49,50]. Unlike conventional BEM, the NURBS basis functions do not obey Kronecker-Delta property, so $\tilde{\mathbf{u}}_A, \tilde{\mathbf{t}}_A$ are not the actual displacement and traction vectors on boundary. And the locations of collocation points (the projection of control points) will influence the stability and accuracy of numerical results. Simpson et al. [50] used Greville abscissae to define collocation points and obtained reasonable and accurate results.

According to Greville abscissae definition, the corresponding parameter of each collocation point is as follows:

$$\bar{\xi}_i = (\xi_i + \xi_{i+1} + \dots + \xi_{i+p})/p, i = 1, 2, \dots, n \quad (15)$$

where p is the order of NURBS basis functions, and n is the number of control points in ξ direction.

If the boundary is discretized into E elements, then the discrete form of Eq. (1) with the absence of body force is as follows

$$\mathbf{C}(\mathbf{x})\mathbf{u}(\mathbf{x}) = \sum_{e=1}^E \int_{S_e} \mathbf{U}(\mathbf{x}, \mathbf{y})\mathbf{t}(\mathbf{y})dS_e - \sum_{e=1}^E \int_{S_e} \mathbf{T}(\mathbf{x}, \mathbf{y})\mathbf{u}(\mathbf{y})dS_e \quad (16)$$

Replacing the continuous fields using NURBS basis functions in Eqs. (13) and (14), Eq. (16) is discretized as follows:

$$C_{ij}(\mathbf{x}(\xi_p)) \sum_{\alpha=1}^N R_{\alpha}^e(\xi_p) \tilde{u}_j^{e\alpha} = \sum_{e=1}^E \sum_{\alpha=1}^N P_{ij}^{e\alpha}(\mathbf{x}, \mathbf{y}) \tilde{t}_j^{e\alpha} - \sum_{e=1}^E \sum_{\alpha=1}^N Q_{ij}^{e\alpha}(\mathbf{x}, \mathbf{y}) \tilde{u}_j^{e\alpha} \quad (17)$$

where

$$P_{ij}^{e\alpha}(\mathbf{x}, \mathbf{y}) = \int_{S_e} U_{ij}(\mathbf{x}(\xi_p), \mathbf{y}(\xi_q)) R_{\alpha}^e(\xi_q) J d\xi_e \quad (18)$$

$$Q_{ij}^{e\alpha}(\mathbf{x}, \mathbf{y}) = \int_{S_e} T_{ij}(\mathbf{x}(\xi_p), \mathbf{y}(\xi_q)) R_{\alpha}^e(\xi_q) J d\xi_e \quad (19)$$

in which $\tilde{u}_j^{e\alpha}$ and $\tilde{t}_j^{e\alpha}$ are the j th components of displacement and traction vectors locating at the α th node of e th element. N denotes the number of the control points corresponding to e th element, and the subscripts p and q are the indexes of source and field points, and J is the Jacobian, which may be calculated by

$$J = \frac{d\Gamma}{d\xi} \quad (20)$$

For each collocation point on the boundary, DBIE is applied to obtain the matrix form of the boundary integral equation as

$$\mathbf{H}\tilde{\mathbf{u}} = \mathbf{G}\tilde{\mathbf{t}} \quad (21)$$

in which $\tilde{\mathbf{u}}$ and $\tilde{\mathbf{t}}$ are vectors containing displacement and traction nodal parameters on control points. \mathbf{H} and \mathbf{G} are the corresponding matrices, whose entries are given as follows:

$$H_{ij}^{e\alpha} = C_{ij}(\mathbf{x}(\xi_p)) \sum_{\alpha=1}^N R_{\alpha}^e(\xi_p) + \sum_{e=1}^E \sum_{\alpha=1}^N Q_{ij}^{e\alpha}(\mathbf{x}(\xi_p), \mathbf{y}(\xi_q)) \quad (22)$$

and

$$G_{ij}^{e\alpha} = \sum_{e=1}^E \sum_{\alpha=1}^N P_{ij}^{e\alpha}(\mathbf{x}(\xi_p), \mathbf{y}(\xi_q)) \quad (23)$$

Considering the known variables on Γ_D and Γ_N , the matrix form of the boundary integral equation can be converted as

$$\mathbf{AX} = \mathbf{F} \quad (24)$$

in which \mathbf{A} is the coefficient matrix, and column matrix \mathbf{X} contains the unknown variables on the boundary. The Telles method and the singularity subtraction technique are common methods to deal with singularities in IGABEM for linear elastic problem [50].

3. IGABEM for viscoelastic problem

BEM has many applications in nonlinear problems such as plasticity [33–35]. The accuracy and correctness of IGABEM for nonlinear problems have been verified [51,52]. In this paper, the viscoelastic boundary integral equation in time domain is derived, and the influence of viscoelastic effect on material properties is shown by the initial stress.

3.1. Constitutive equation

The constitutive model of linear thermoviscoelastic materials can be described by Stieltjes integral [53],

$$\sigma_{ij}(\mathbf{x}, t) = \delta_{ij} \int_{-\infty}^t [K(\gamma - \gamma') - \frac{2}{3}G(\gamma - \gamma')] \frac{\partial \varepsilon_{kk}(\mathbf{x}, t')}{\partial t'} dt' + 2 \int_{-\infty}^t G(\gamma - \gamma') \frac{\partial \varepsilon_{ij}(\mathbf{x}, t')}{\partial t'} dt' \quad (25)$$

in which K and G mean the bulk modulus and shear modulus, respectively. And γ is reduced time caused by temperature, which can be described as

$$\gamma(t) = \int_0^t \frac{d\tau}{a_T[T(\mathbf{x}, \tau)]} \quad (26)$$

where τ is an arbitrary real variable in the interval $[0, t]$. This equation was proposed by Morland and Lee [54] for the case of transient temperature conditions. Williams et al. [55] proposed an empirical formula, known as WLF (William–Landel–Ferry) equation

$$\log a_T = \frac{-C_1(\Theta - \Theta_{ref})}{C_2 + \Theta + \Theta_{ref}} \quad (27)$$

where C_1 and C_2 are material constants that depend on the chosen reference temperature Θ_{ref} .

Assuming the object is on the state of free-stress when $t < 0$, then the stress in Eq. (25) can be divided into two parts (elastic stress and memory stress) as follows [53]:

$$\sigma_{ij}(\mathbf{x}, t) = \sigma_{ij}^e(\mathbf{x}, t) - \sigma_{ij}^m(\mathbf{x}, t) \quad (28)$$

in which,

$$\sigma_{ij}^e(\mathbf{x}, t) = \delta_{ij}[K(0) - \frac{2}{3}G(0)]\varepsilon_{kk}(\mathbf{x}, t) + 2G(0)\varepsilon_{ij}(\mathbf{x}, t) \quad (29)$$

$$\begin{aligned} \sigma_{ij}^m(\mathbf{x}, t) = & 2 \int_0^t \frac{\partial G(\xi - \xi')}{\partial t'} \varepsilon_{ij}(\mathbf{x}, t') dt' + \delta_{ij} \int_0^t \frac{\partial K(\xi - \xi')}{\partial t'} \varepsilon_{kk}(\mathbf{x}, t') dt' \\ & - \delta_{ij} \frac{2}{3} \int_0^t \frac{\partial G(\xi - \xi')}{\partial t'} \varepsilon_{kk}(\mathbf{x}, t') dt' \end{aligned} \quad (30)$$

where there are general integral relations in Eq. (30). We use Prony series to describe the relaxation elastic modulus, and the specialized discretization process can be found in [Appendix A](#).

3.2. Boundary-domain integral equation for viscoelastic problem [56]

Considering the viscoelastic problem, the memory stress can be regarded as pseudo body force and boundary traction instead of the traditional form in Eq. (1) as follows:

$$b'_j = -\sigma_{ij,j}^m + b_j \quad (31)$$

and

$$t'_i = t_i + \sigma_{ij}^m n_j \quad (32)$$

Replacing the body force and boundary traction by Eqs. (31) and (32), the boundary-domain integral equation (1) can be written as

$$C_{ij} u_j = \int_{\Gamma} U_{ij} t_j d\Gamma + \int_{\Gamma} U_{ij} \sigma_{kj}^m n_k d\Gamma - \int_{\Gamma} T_{ij} u_j d\Gamma + \int_{\Omega} U_{ij} b_j d\Omega - \int_{\Omega} U_{ij} \sigma_{kj,k}^m d\Omega \quad (33)$$

According to Gauss's divergence theory, Eq. (33) can be converted as

$$\int_{\Gamma} U_{ij} \sigma_{kj}^m n_k d\Gamma - \int_{\Omega} U_{ij} \sigma_{kj,k}^m d\Omega = \int_{\Omega} U_{ij,k} \sigma_{kj}^m d\Omega \quad (34)$$

Considering the symmetry of stress σ_{kj} about the subscripts of k and j , one has

$$\begin{aligned}\int_{\Omega} U_{ij,k} \sigma_{kj}^m d\Omega &= \int_{\Omega} \frac{1}{2} (U_{ij,k} + U_{ik,j}) \sigma_{kj}^m d\Omega \\ &= \int_{\Omega} B_{ijk} \sigma_{jk}^m d\Omega\end{aligned}\quad (35)$$

In general, taking the memory stress as initial stress, the boundary-domain integral formula for viscoelastic problem can be described as

$$C_{ij} u_j = \int_{\Gamma} U_{ij} t_j d\Gamma - \int_{\Gamma} T_{ij} u_j d\Gamma - \int_{\Omega} B_{ijk} \sigma_{jk}^m d\Omega + \int_{\Omega} U_{ij} b_j d\Omega \quad (36)$$

in which B_{ijk} is the kernel function corresponding to a strain component as

$$\begin{aligned}B_{ijk} &= \frac{1}{2} (U_{ij,k} + U_{ik,j}) \\ &= \frac{1}{16\pi G(1-v)} \frac{1}{r} \{(3-4v)(r_{,k}\delta_{ij} + r_{,j}\delta_{ik}) - 2\delta_{jk}r_{,i} \\ &\quad - \delta_{ij}r_{,k} - \delta_{ik}r_{,j} + 4r_{,i}r_{,j}r_{,k}\}\end{aligned}\quad (37)$$

In the absence of body force, the displacement boundary-domain integral equation (DBIE) for viscoelastic problem in Eq. (36) can be converted as

$$C_{ij} u_j = \int_{\Gamma} U_{ij} t_j d\Gamma - \int_{\Gamma} T_{ij} u_j d\Gamma - \int_{\Omega} B_{ijk} \sigma_{jk}^m d\Omega \quad (38)$$

Similarly, the boundary-domain integral equation for internal points has the same form with Eq. (37) as

$$u_i = \int_{\Gamma} U_{ij} t_j d\Gamma - \int_{\Gamma} T_{ij} u_j d\Gamma - \int_{\Omega} B_{ijk} \sigma_{jk}^m d\Omega \quad (39)$$

Based on small deformation theory, we can obtain the strain boundary-domain integral equation as

$$\begin{aligned}\varepsilon_{ij}(p) &= \frac{1}{2} \left(\frac{\partial u_i(p)}{\partial x_j^p} + \frac{\partial u_j(p)}{\partial x_i^p} \right) \\ &= \int_{\Gamma} \bar{U}_{ijk}^*(p, q) t_k(q) d\Gamma(q) - \int_{\Gamma} \bar{T}_{ijk}^*(p, q) u_k(q) d\Gamma(q) \\ &\quad - \int_{\Omega-B} \xi_{ijkl}^*(p, q) \sigma_{lk}^m(q) d\Omega(q) + F_{ij}(p)\end{aligned}\quad (40)$$

Due to the singularity of the domain integral in Eq. (40), the solution can be derived as an additional value F_{ij} about the small circle B , which can be expressed as

$$F_{ij}(p) = -\frac{1}{16(1-v)G} [2(3-4v)\sigma_{ij}^m(p) - \delta_{ij}\sigma_{rr}^m(p)] \quad (41)$$

and the kernel functions of the strain boundary-domain integral equation for viscoelastic problem are given as

$$\begin{aligned}\bar{U}_{ijk}^* &= \frac{1}{2} \left(\frac{\partial U_{ik}}{\partial x_j^p} + \frac{\partial U_{jk}}{\partial x_i^p} \right) \\ &= \frac{1}{16\pi G(1-v)} \frac{1}{r} \{(3-4v)(r_{,i}\delta_{jk} + r_{,j}\delta_{ik}) - 2\delta_{ij}r_{,k} - \delta_{jk}r_{,i} - \delta_{ik}r_{,j} + 4r_{,i}r_{,j}r_{,k}\}\end{aligned}\quad (42)$$

$$\begin{aligned}\bar{T}_{ijk}^* &= \frac{1}{2} \left(\frac{\partial T_{ik}}{\partial x_j^p} + \frac{\partial T_{jk}}{\partial x_i^p} \right) \\ &= A_1 \frac{1}{r^2} \left\{ \frac{\partial r}{\partial n} [(B_1 - 1)(\delta_{ik}r_{,j} + \delta_{jk}r_{,i}) - 2\delta_{ij}r_{,k} + 8r_{,i}r_{,j}r_{,k}] - [B_1\delta_{jk} + (1 - B_1)r_{,j}r_{,k}]n_i \right. \\ &\quad \left. - [B_1\delta_{ik} + (1 - B_1)r_{,i}r_{,k}]n_j + B_1(\delta_{ij} - 2r_{,i}r_{,j})n_k \right\}\end{aligned}\quad (43)$$

and

$$\begin{aligned}\xi_{ijkl}^* &= \frac{1}{2} \left(\frac{\partial B_{ilk}}{\partial x_j^p} + \frac{\partial B_{jlk}}{\partial x_i^p} \right) \\ &= \frac{A_2}{4r^2} \{ 2(B_2 - 1)(\delta_{il}r_{,j}r_{,k} + \delta_{ik}r_{,j}r_{,i} + \delta_{jl}r_{,i}r_{,k} + \delta_{jk}r_{,i}r_{,l}) - 8\delta_{lk}r_{,i}r_{,j} \\ &\quad - 2(B_2 - 1)(\delta_{ik}\delta_{jl} + \delta_{il}\delta_{jk}) + 4\delta_{ij}\delta_{lk} - 4(2\delta_{ij}r_{,l}r_{,k} + \delta_{jl}r_{,i}r_{,k} + \delta_{jk}r_{,i}r_{,l} \\ &\quad + \delta_{il}r_{,j}r_{,k} + \delta_{ik}r_{,j}r_{,i}) + 32r_{,i}r_{,j}r_{,l}r_{,k} \}\end{aligned}\quad (44)$$

in which $A_1 = -\frac{1}{4\pi(1-v)}$, $B_1 = (1-2v)$ and $A_2 = \frac{1}{8\pi G(1-v)}$, $B_2 = (3-4v)$.

According to the linear elastic constitutive equation (29), the stress boundary-domain integral equation at the inner point p is given as

$$\begin{aligned}\sigma_{ij}^e(p) &= \int_{\Gamma} D_{ijk}(p, q)t_k(q)d\Gamma(q) - \int_{\Gamma} S_{ijk}(p, q)u_k(p, q)d\Gamma(q) \\ &\quad - \int_{\Omega-B} R_{ijkl}(p, q)\sigma_{lk}^m(q)d\Omega(q) + \bar{F}_{ij}(p)\end{aligned}\quad (45)$$

in which

$$\bar{F}_{ij}(p) = -\frac{1}{8(1-v)}[(6-8v)\sigma_{ij}^m(p) - (1-4v)\sigma_{rr}^m(p)\delta_{ij}] \quad (46)$$

and

$$\begin{cases} D_{ijk} = 2G(0)\bar{U}_{ijk}^* + \delta_{ij}[K(0) - \frac{2}{3}G(0)]\bar{U}_{rrk}^* \\ S_{ijk} = 2G(0)\bar{T}_{ijk}^* + \delta_{ij}[K(0) - \frac{2}{3}G(0)]\bar{T}_{rrk}^* \\ R_{ijkl} = 2G(0)\xi_{ijkl}^* + \delta_{ij}[K(0) - \frac{2}{3}G(0)]\xi_{rrlk}^* \end{cases} \quad (47)$$

It is noticeable that the kernel functions are all related to shear and bulk modules at $t = 0$, which means that the time only affects the domain integral part related to the memory stress in Eqs. (36), (40) and (45).

3.3. Regularized boundary integral equation

The singularity of integrals in BEM is the key point to be solved, which will greatly influence the accuracy and effectiveness of the algorithm. Regularized boundary integral equation based on the addition and subtraction technique [57] can be used to reduce the singular order of integrals.

Take the domain integral in Eq. (40) as an example. Extracting the singular term in the integral representation of memory stress, we obtain regularized integral representation of the singular domain integral

$$\begin{aligned}&\int_{\Omega} \xi_{ijkl}^*(p, q)\sigma_{lk}^m(q)d\Omega(q) \\ &= \int_{\Omega} \xi_{ijkl}^*(p, q)[\sigma_{lk}^m(q) - \sigma_{lk}^m(p)]d\Omega(q) + \int_{\Omega} \xi_{ijkl}^*(p, q)\sigma_{lk}^m(p)d\Omega(q) \\ &= \int_{\Omega} \xi_{ijkl}^*(p, q)[\sigma_{lk}^m(q) - \sigma_{lk}^m(p)]d\Omega(q) - \frac{1}{2}\sigma_{lk}^m(p) \int_{\Gamma_{\Omega}} [B_{ilk}(p, Q)n_j + B_{jlk}(p, Q)n_i]d\Gamma(Q)\end{aligned}\quad (48)$$

where Γ_{Ω} is the boundary of domain Ω , and similar procedure can be repeated also for the domain integral in Eq. (45).

Therefore, substituting Eq. (48) into Eq. (40), we can obtain the regularized strain integral equation,

$$\begin{aligned}\varepsilon_{ij}(p) &= \int_{\Gamma} \bar{U}_{ijk}^*(p, q)t_k(q)d\Gamma(q) - \int_{\Gamma} \bar{T}_{ijk}^*(p, q)u_k(q)d\Gamma(q) \\ &\quad - \int_{\Omega} \xi_{ijkl}^*(p, q)[\sigma_{lk}^m(q) - \sigma_{lk}^m(p)]d\Omega(q) + \frac{1}{2}\sigma_{lk}^m(p) \int_{\Gamma_{\Omega}} [B_{ilk}(p, Q)n_j + B_{jlk}(p, Q)n_i]d\Gamma(Q)\end{aligned}\quad (49)$$

It is worthy noticing that the Cauchy principal value integral $F_i(p)$ and $\bar{F}_{ij}(p)$ will be eliminated by the addition and subtraction technique [58] through the opposite direction integral around the small circle B of source point in Eqs. (40) and (45).

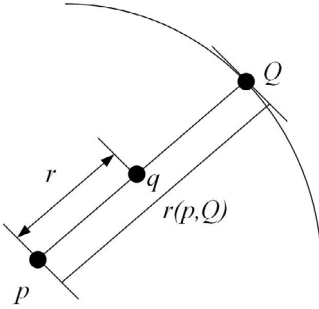


Fig. 2. Radial integral method.

3.4. Transformation of domain integrals to the boundary integrals using RIM

Since the existence of domain integrals will eliminate the advantage of only boundary discretization for BEM, in this section, the two integrals involved in Eqs. (38) and (49) are transformed into equivalent boundary integrals by using the RIM proposed by Gao [36]. Here, we give some details about RIM and explain how to deal with singular integrals based on this method. The unknown variables including memory stress are expressed as a combination of radial basis functions and polynomials in global coordinate,

$$\sigma_{jk}^m(q) = \sum_{A=1}^N a_{jk}^A \phi^A(R) + C_{jk}^0 + \sum_{\mu=1}^m C_{jk}^\mu x_\mu \quad (50)$$

and

$$\sum_{A=1}^N a_{jk}^A = \sum_{A=1}^N a_{jk}^A x_\mu = 0 \quad (51)$$

where A is applied points consisting of all boundary nodes and internal points. $N = N_b + N_I$ is the number of the applied points, in which N_b is the number of boundary points and N_I is the number of inner points. The parameters on the boundary points can be obtained from Appendix B. The coefficients a_{jk}^A , C_{jk}^0 and C_{jk}^μ are determined by the coordinates of all applied points. m indicates the dimension of the considered problems. ϕ^A is the radial basis function (RBF). In order to balance the accuracy and stability of numerical results, 4th order spline-type RBF [59] is used and its expression is given as follows

$$\phi(R_i/d_i) = \begin{cases} 1 - 6(\frac{R_i}{d_i})^2 + 8(\frac{R_i}{d_i})^3 - 3(\frac{R_i}{d_i})^4, & 0 \leq R_i \leq d_i \\ 0, & d_i \leq R_i \end{cases} \quad (52)$$

where d_i is the support size.

By applying RBF directly to the domain integral $\int_{\Omega} B_{ijk}(p, q) \sigma_{jk}^m(q) d\Omega$, the following formula can be obtained

$$\begin{aligned} & \int_{\Omega} B_{ijk}(p, q) \sigma_{jk}^m(q) d\Omega \\ &= \int_{\Gamma} \frac{1}{r} \frac{dr}{dn} \left[\int_0^{r(p, Q)} B_{ijk}^*(p, q) \sigma_{jk}^m(q) r dr \right] d\Gamma \\ &= \int_{\Gamma} \frac{1}{r} \frac{dr}{dn} \left[\int_0^{r(p, Q)} B_{ijk}^*(p, q) \left(\sum_{A=1}^N a_{jk}^A \phi^A(q) + C_{jk}^0 + \sum_{\mu=1}^m C_{jk}^\mu x_\mu \right) r dr \right] d\Gamma \end{aligned} \quad (53)$$

As shown in Fig. 2, the domain integral can be converted into a combination about boundary integral between source point p and boundary point Q and radial integral between source point p and field point q . The weakly singular integral with order $O(1/r)$ for the boundary integral in Eq. (53) can be solved through Telles method [50] as mentioned in Section 1.

Substituting Eq. (50) into domain integral $\int_{\Omega} \xi_{ijkl}^*(p, q)[\sigma_{lk}^m(q) - \sigma_{lk}^m(p)]d\Omega(q)$, we can obtain the following equation

$$\begin{aligned} & \int_{\Omega} \xi_{ijkl}^*(p, q)[\sigma_{lk}^m(q) - \sigma_{lk}^m(p)]d\Omega(q) \\ &= a_{jk}^A \int_{\Gamma} \frac{1}{r} \frac{\partial r}{\partial n} F_{ijkl}^A(p, Q)d\Gamma(Q) \\ &+ C_{jk}^0 \int_{\Gamma} \frac{1}{r} \frac{\partial r}{\partial n} F_{ijkl}^0(p, Q)d\Gamma(Q) \\ &+ C_{jk}^{\mu} \int_{\Gamma} \frac{1}{r} \frac{\partial r}{\partial n} F_{ijkl}^{\mu}(p, Q)d\Gamma(Q) \end{aligned} \quad (54)$$

in which

$$\begin{cases} F_{ijkl}^A(p, Q) = \int_0^{r(p, Q)} \xi_{ijkl}^*(p, q)[\phi^A(q) - \phi^A(p)]rdr \\ F_{ijkl}^0(p, Q) = 0 \\ F_{ijkl}^{\mu}(p, Q) = \int_0^{r(p, Q)} \xi_{ijkl}^*(p, q)[x_{\mu}(q) - x_{\mu}(p)]rdr \end{cases} \quad (55)$$

Apparently, there are no singularities on radial integral in Eq. (55), and the singularity for the boundary integral in Eq. (54) will disappear when the source points are not on the boundary Γ . Due to the same singularity, the stress boundary-domain integral equation (45) can be treated in the same way. More details about this transformation relation can be found in [36].

3.5. Isogeometric implementation of the regularized boundary integral equations

In this work, the IGABEM is adopted to study this viscoelastic problem for solid propellant. Notice that there are the same forms between linear elastic problem and viscoelastic problem except for the domain integral caused by the initial stress, i.e. memory stress. Then, we focus on the isogeometric analysis on the domain integrals in Eqs. (53) and (54) as follows

$$\begin{aligned} & \int_{\Omega} B_{ijk}(p, q)\sigma_{jk}^m(q)d\Omega \\ &= \sum_{e=1}^E \sum_{a=1}^N \int_{-1}^1 \frac{1}{r^{(p, Q)}} \frac{\partial r}{\partial n} \left[\int_0^{r(p, Q)} B_{ijk}(p, q) \left(\sum_{A=1}^N a_{jk}^A \phi^A(q) + C_{jk}^0 + \sum_{\mu=1}^m C_{jk}^{\mu} x_{\mu} \right) r dr \right] J(\xi) d\xi \end{aligned} \quad (56)$$

and

$$\begin{aligned} & \int_{\Omega} \xi_{ijkl}^*(p, q)[\sigma_{lk}^m(q) - \sigma_{lk}^m(p)]d\Omega(q) \\ &= a_{jk}^A \sum_{e=1}^E \sum_{a=1}^N \int_{-1}^1 \frac{1}{r^{(p, Q)}} \frac{\partial r}{\partial n} F_{ijkl}^A(p, Q) J(\xi) d\xi \\ &+ C_{jk}^0 \sum_{e=1}^E \sum_{a=1}^N \int_{-1}^1 \frac{1}{r^{(p, Q)}} \frac{\partial r}{\partial n} F_{ijkl}^0(p, Q) J(\xi) d\xi \\ &+ C_{jk}^{\mu} \sum_{e=1}^E \sum_{a=1}^N \int_{-1}^1 \frac{1}{r^{(p, Q)}} \frac{\partial r}{\partial n} F_{ijkl}^{\mu}(p, Q) J(\xi) d\xi \end{aligned} \quad (57)$$

After integration, the discrete boundary-domain integration equations (38) and (40) can be written as the following matrix forms

$$\mathbf{H}\tilde{\mathbf{u}} = \mathbf{G}\tilde{\mathbf{t}} + \mathbf{B} \quad (58)$$

$$\boldsymbol{\varepsilon} = \mathbf{H}^{\varepsilon} \tilde{\mathbf{u}} + \mathbf{G}^{\varepsilon} \tilde{\mathbf{t}} + \mathbf{B}^{\varepsilon} \quad (59)$$

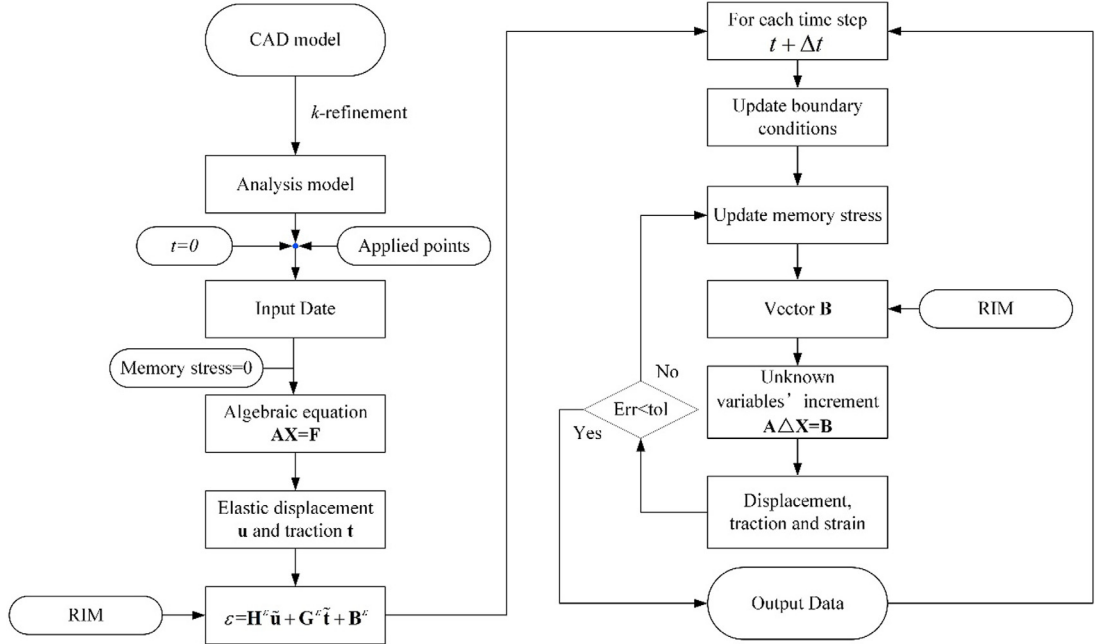


Fig. 3. Iteration algorithm for viscoelastic boundary element method.

Meanwhile, considering the known variables on Γ_D and Γ_N , the matrix form of the boundary-domain integral equation (58) can be converted as

$$\mathbf{AX} = \mathbf{F} + \mathbf{B} \quad (60)$$

in which \mathbf{A} , \mathbf{X} and \mathbf{F} own the same meanings with the matrices in Eq. (24).

4. Iteration process

Assuming the object is on the stress-free state when $t < 0$, the material parameters in coefficient matrix \mathbf{A} will keep the values at $t = 0$, which means that the coefficient matrix \mathbf{A} remains the same in the iteration process. This feature is helpful to save computational time in the iteration process.

The iterative method is adopted to obtain the objective value until the numerical results converge. The process of the viscoelastic boundary element method is shown in Fig. 3.

where the value of t_0 depends on the definition of the stress-free state, t_i is the discretized time points, and it can be obtained from Appendix A. $\Delta\mathbf{X}$ is the increment vector of the unknown variable vector caused by the domain integral in Eq. (56). tol means the convergence criteria. Err is the relative error and its definition can be found in Eq. (61).

5. Numerical examples

In this section, we shall examine five numerical examples in 2D plane strain problem to show the correctness of the IGABEM based on RIM for solving viscoelastic problems. The exact solutions derived from correspondence principle in Appendix C are employed to examine the computational results in the present method. There are not accurate principles about time interval and the number of applied points in RIM, so we use numerical experiments to demonstrate their impacts on numerical accuracy. To avoid the influence of convergence error, the relative error between different iteration processes is given as

$$Err = \left\| \frac{\Delta\mathbf{X}_{n+1}}{\mathbf{X} + \Delta\mathbf{X}_n} \right\|_2 < tol = 10^{-5} \quad (61)$$

in which n is the iteration time, and \mathbf{X} and $\Delta\mathbf{X}$ can be found in Fig. 3.

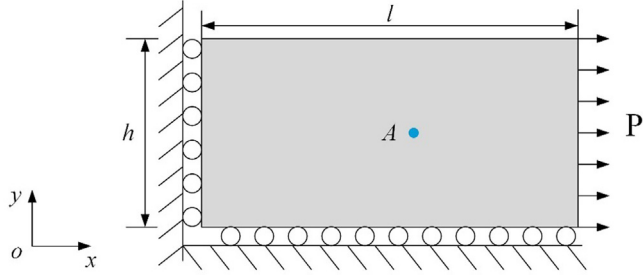


Fig. 4. The problem description about the stressed bar.

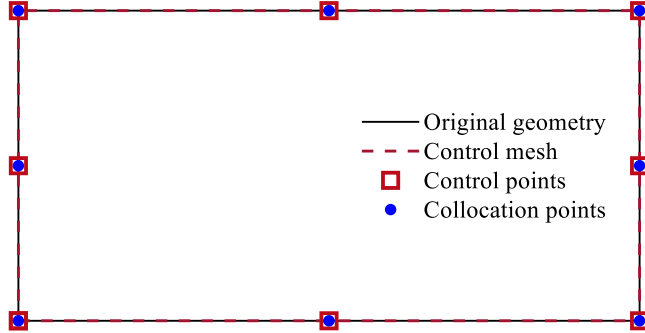


Fig. 5. CAD model of the stressed bar.

From the macro mechanic, the solid propellant is the homogeneous and isotropic viscoelastic material and its behaviors can be simulated from Sections 5.1–5.4. However, the solid propellant is polymer containing up to 86%–90% elastic solid particles from the micro mechanic and the distribution of solid particles is random. Because the existence of solid particles will influence the structure integrity of solid propellant grains, we discuss how to simulate the micro structure of solid propellant and its behaviors in Section 5.5.

5.1. Simple tension bar

The simple bar depicted in Fig. 4 is analyzed when a force is exerted on its free end. The geometrical dimensions of the bar are $l = 10$ and $h = 5$. The loading on the right boundary is given as follows

$$P(t) = 100H(t); \quad (62)$$

where the definition of the unit step function $H(t)$ is defined as

$$H(t - t_0) = \begin{cases} 0 & \text{for } t < t_0 \\ 1 & \text{for } t > t_0 \end{cases} \quad (63)$$

The viscoelastic material parameters can be described by Prony-series [60],

$$G(t) = 100 + 9900 \exp(-2.3979t) \quad (64)$$

$$K(t) = K(0) = 20000 \quad (65)$$

The coordinate of the monitor point A is $(6, 2.5)$. The order p of NURBS is 2, and the knot vector for the CAD model in Fig. 5 is

$$\Xi = \{0, 0, 0, 1, 1, 2, 2, 3, 3, 4, 4, 4\} \quad (66)$$

The analysis model is obtained for CAD model after 3 h -refinements.

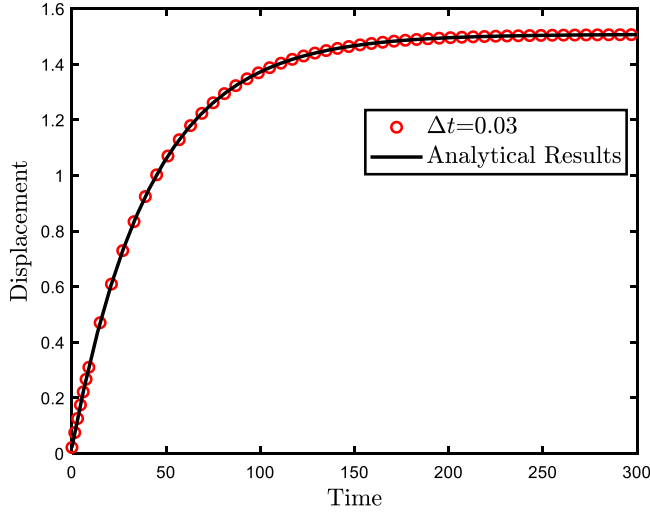


Fig. 6. Displacements in terms of time.

The number of applied points will not influence the accuracy of RIM because of the uniform distribution of strain on the whole bar, so we just use the monitor point A as inner point. In order to facilitate us to explore the effect of time interval Δt , five-time intervals are used, namely 0.03, 0.3, 0.8, 1 and 3. Fig. 6 shows an excellent consistence between numerical results and analytical results under the time interval $\Delta t = 0.03$. As shown in Fig. 7, the error increases with the time interval. Because the time interval is related to the computing time, too small-time interval will reduce the computational efficiency. Here, we choose the combination of different time intervals to simulate the creep behavior of viscoelastic materials as follows

$$\Delta t = \begin{cases} 0.03, & 0 \leq t < 30 \\ 0.3, & 30 \leq t < 50 \\ 0.8, & 50 \leq t < 100 \\ 1.0, & 100 \leq t < 200 \\ 3.0, & 200 \leq t < 300 \end{cases} \quad (67)$$

Compared to Fig. 7, Fig. 8 shows a more accurate result. It is important to develop a standard for this changed time interval strategy to balance numerical accuracy with computational efficiency.

There are three common features for viscoelastic materials: creep, relaxation and recovery. Figs. 7 and 8 describe the creep experiments for viscoelastic materials. Choose the time interval $\Delta t = 0.03$ to obtain more accurate results and assume another loading on the free end as

$$P(t) = 100H(t) - 100H(t - 100) \quad (68)$$

in which the outer loading on the right side will be 100 when $t \leq 100$, and it will be zero when $t > 100$. This numerical test can be used to show the recovery of the viscoelastic materials. As shown in Fig. 9, the rapid decline of the displacement of the monitor point at $t = 100$ reflects the linear elastic properties in Eq. (29). Meanwhile, Fig. 9 demonstrates the effectiveness and robustness of this numerical algorithm to simulate the creep and recovery behaviors of viscoelastic materials.

5.2. A thick-walled cylinder under pressure

The RIM and traditional cell discretization method are two common methods to deal with volume integral. In this section, a thick-walled cylinder subjected to an internal pressure P is analyzed. In order to evaluate the influence from the number and position of applied points in RIM, a sensitivity analysis and the comparison between RIM

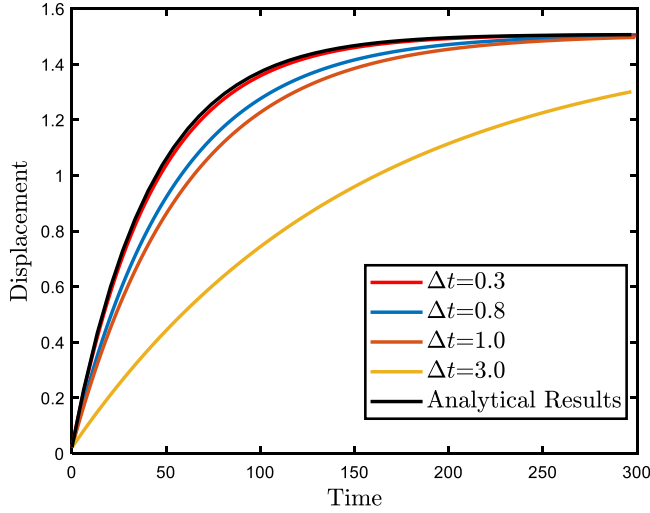


Fig. 7. The influence of the length of time step.

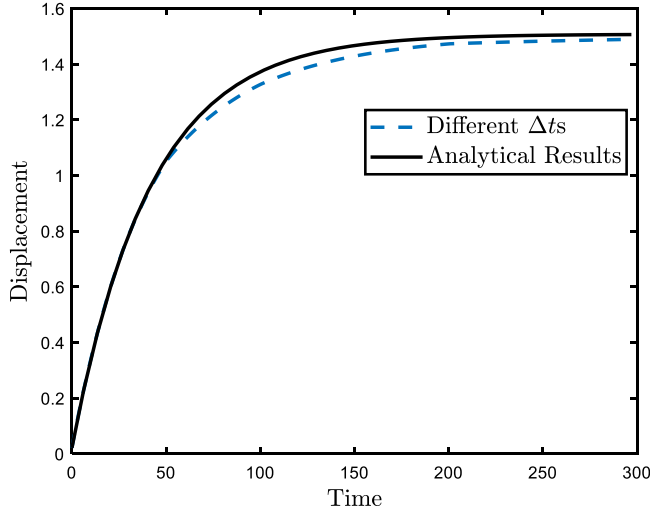


Fig. 8. Numerical results obtained from a combination of different time intervals.

and traditional cell discretization are applied. As shown in Fig. 10, the outer boundary radius and inner radius of the cylinder are $a = 10$ and $b = 5$, respectively. The material parameters are the same as those in Eqs. (64) and (65). Considering the symmetry of the problem, the discretization of the object is reduced, as shown in Fig. 11.

5.2.1. RIM for volume integral

In this section, the analysis model is obtained from CAD model after 9 h -refinements. The effect of the number of the applied points on the results is discussed. As shown in Fig. 12, four computational models are used with the same control points and different numbers of internal points, which are 9, 25, 64 and 200. The simple geometry makes it possible to put inner points in the domain evenly.

The time interval is $\Delta t = 0.03$, the monitor point is set on the arbitrary point with radius $r = 7.5$. Fig. 13 shows the influence of the number and position of inner points in RIM, which demonstrates that the number of inner points will affect the accuracy of this algorithm. This is due to RIM's accuracy, and its error increases with the increase of memory stress. Obviously, the accuracy of RIM can increase with the number of inner points, but when the inner points are very close to the boundary, nearly singular integrals in Eq. (40) will be generated. This question should

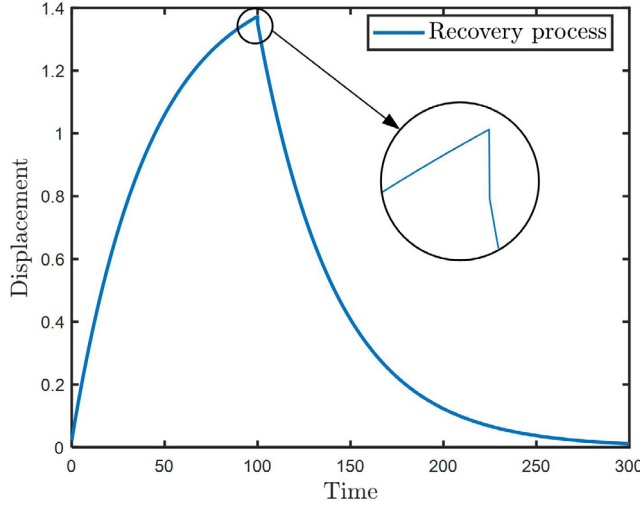


Fig. 9. The creep and recovery processes in terms of time.

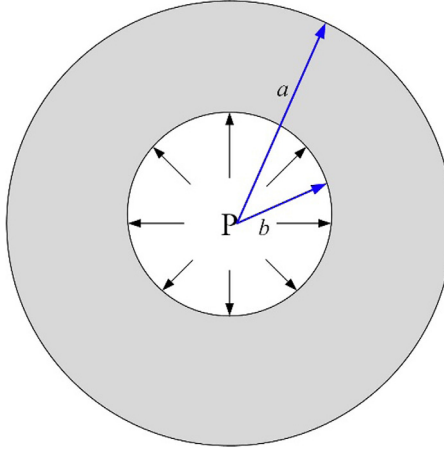


Fig. 10. Thick-walled cylinder model.

be handled with caution in the future work. [Fig. 14](#) shows the stress distribution of the cylinder under the condition that it does not change with time, and the analytical results can be found in [\[60\]](#).

5.2.2. Cell discretization for volume integral

As shown in [Fig. 13](#), the number and the position of inner points will influence the numerical accuracy. However, it is still unclear that it is due to the use of radius basis function or the feature of the viscoelastic problem. Here, we use cell discretization to deal with volume integrals and compare their numerical results with those from RIM. The CAD model for cell discretization is obtained from IGAFEM as shown in [Fig. 15](#), in which there are the same boundary points as shown in [Fig. 11](#). The singular integrals in volume integrals can be disposed by the regularized boundary integral equations in Section 3.3 and the element sub-division method [\[61\]](#). The analysis models are respectively obtained from 3, 5, 7 and 9 h -refinements as shown in [Fig. 16](#), in which the boundary points and inner points as applied points are used in RIM simultaneously. This strategy can keep the same accuracy for the boundary integral part, in which the number of Gauss quadrature points is set to 20. Meanwhile, the number of Gauss quadrature points for volume integrals using cell discretization method is set to 3×3 .

The monitor point is set on the arbitrary point with radius $r = 7.7061$. In order to balance the computational efficiency and numerical accuracy, the combination of different time intervals is applied to simulate the creep

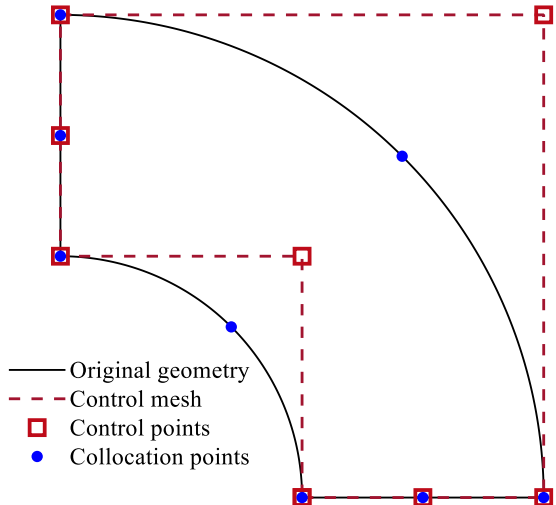


Fig. 11. CAD model in IGABEM for thick-walled cylinder and its basic parameters: the knot vector $\Xi = \{0, 0, 0, 1, 1, 2, 2, 3, 3, 4, 4, 4\}$ and the weights $\omega = \{1, \frac{\sqrt{2}}{2}, 1, \frac{\sqrt{2}}{2}, 1, \frac{\sqrt{2}}{2}, 1, \frac{\sqrt{2}}{2}, 1\}$.

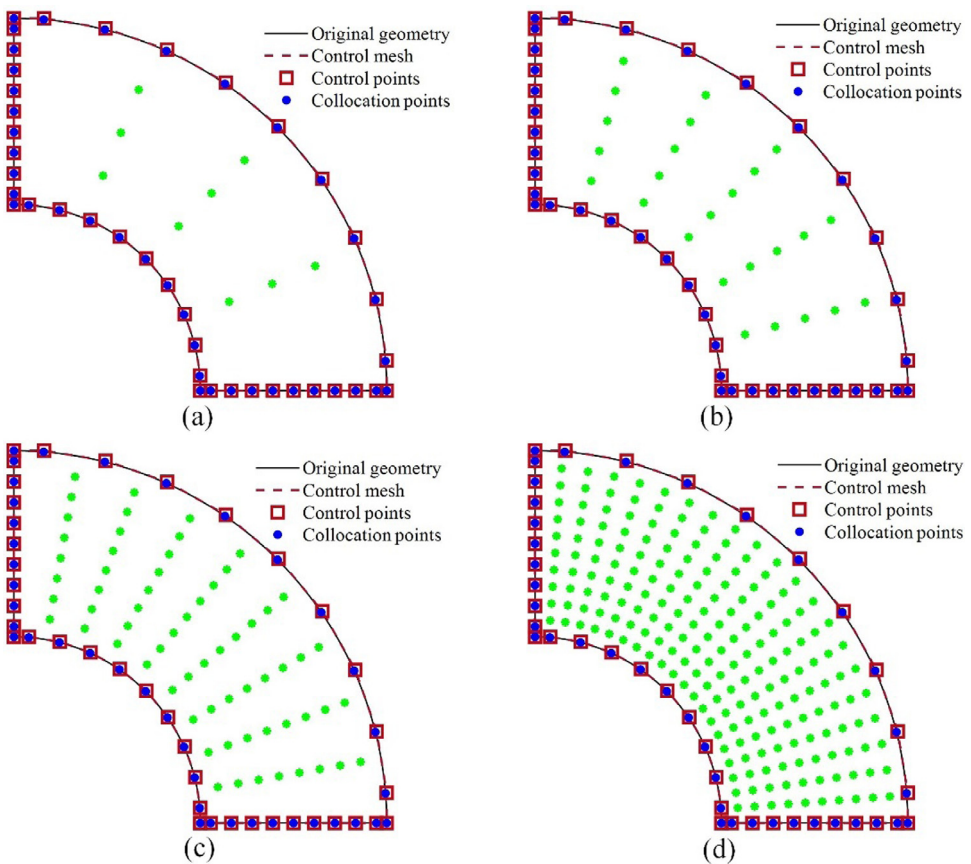


Fig. 12. Computational models with different internal applied points: (a) $N_I = 9$; (b) $N_I = 25$; (c) $N_I = 64$; (d) $N_I = 200$.

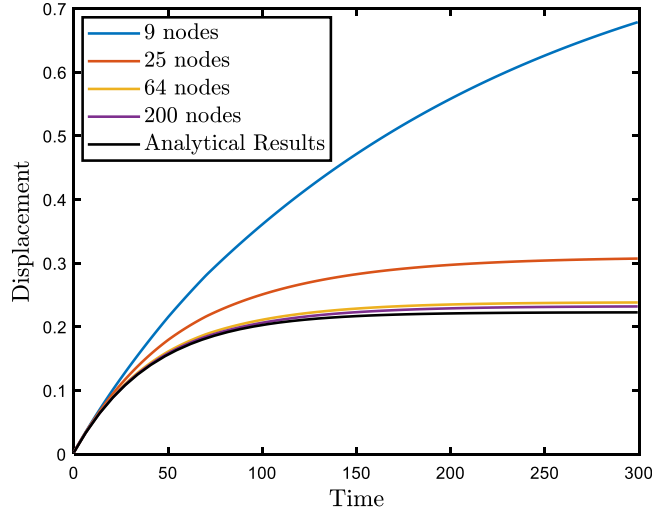


Fig. 13. Different displacements under four numbers of inner points.

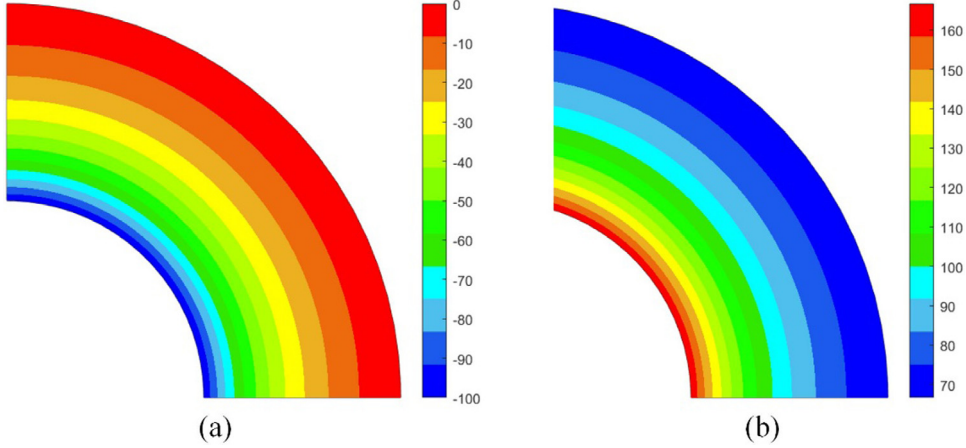


Fig. 14. Stress distribution: (a) Radial stress; (b) Tangential stress.

behavior of viscoelastic materials as follows

$$\Delta t = \begin{cases} 0.03, & 0 \leq t < 5 \\ 0.05, & 5 \leq t < 10 \\ 0.08, & 10 \leq t < 20 \\ 0.15, & 20 \leq t < 50 \\ 0.3, & 50 \leq t < 70 \\ 0.5 & 70 \leq t < 300 \end{cases} \quad (69)$$

The convergence of numerical results obtained from the analysis models in Fig. 16 can be found in Fig. 17 in terms of refinement time. However, the numerical results from RI-IGABEM in Fig. 17(d) have less accuracy than those in Fig. 17(c). We use the same inner points and the boundary points obtained from 12 h -refinements as shown in Fig. 18(a) to stimulate the creep behavior through RI-IGABEM, and this kind of numerical results in Fig. 18(b) owns better numerical accuracy than those in Fig. 17(c). This phenomenon demonstrates that the number and position of inner points will influence the numerical accuracy both in the RIM and in the cell discretization

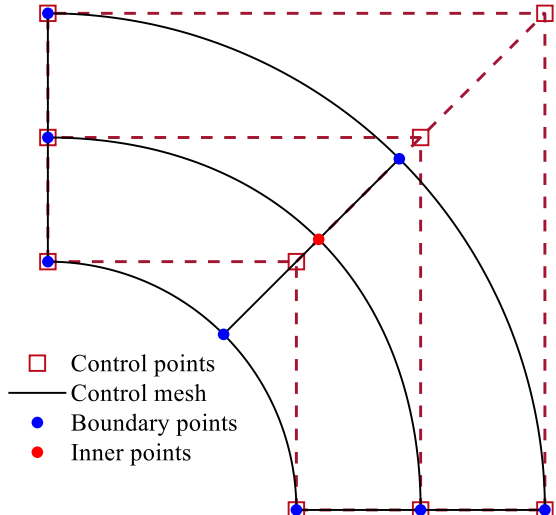


Fig. 15. CAD model in IGAFEM for thick-walled cylinder and its basic parameters: the knot vector $\Xi_1 = \Xi_2 = \{0, 0, 0, 1, 1, 1\}$ and the weights $\omega = \{1, \frac{\sqrt{2}}{2}, 1, \frac{\sqrt{2}}{2}, 1, \frac{\sqrt{2}}{2}, 1\}$.

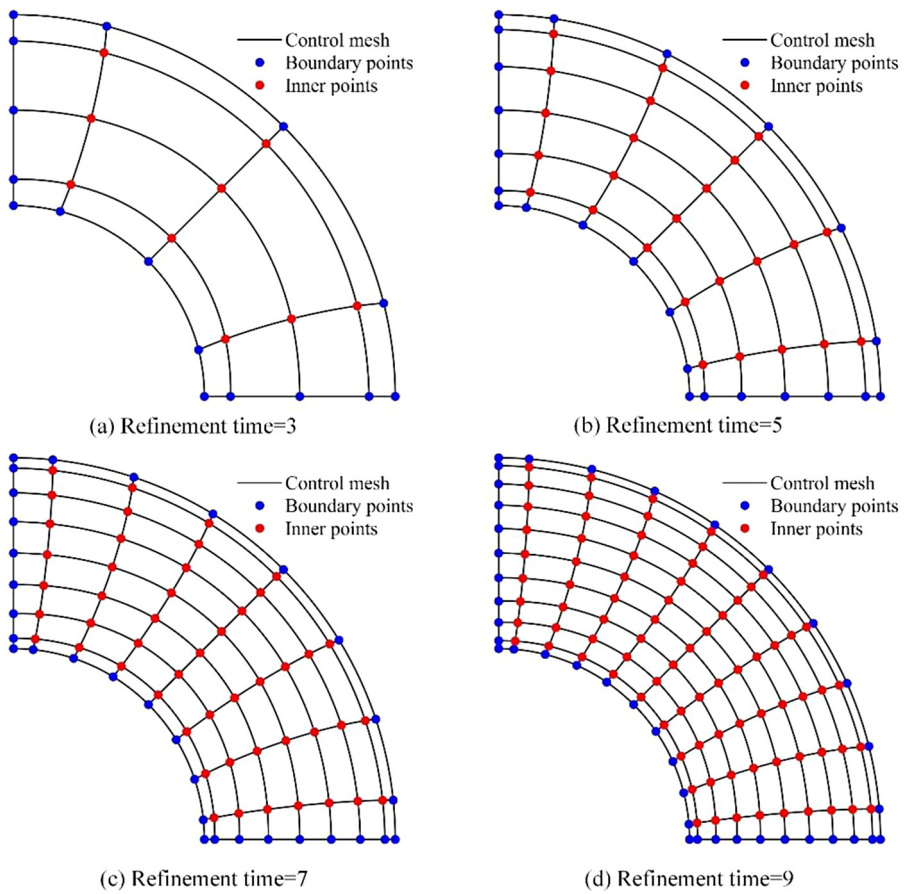


Fig. 16. The analysis models from different h -refinements.

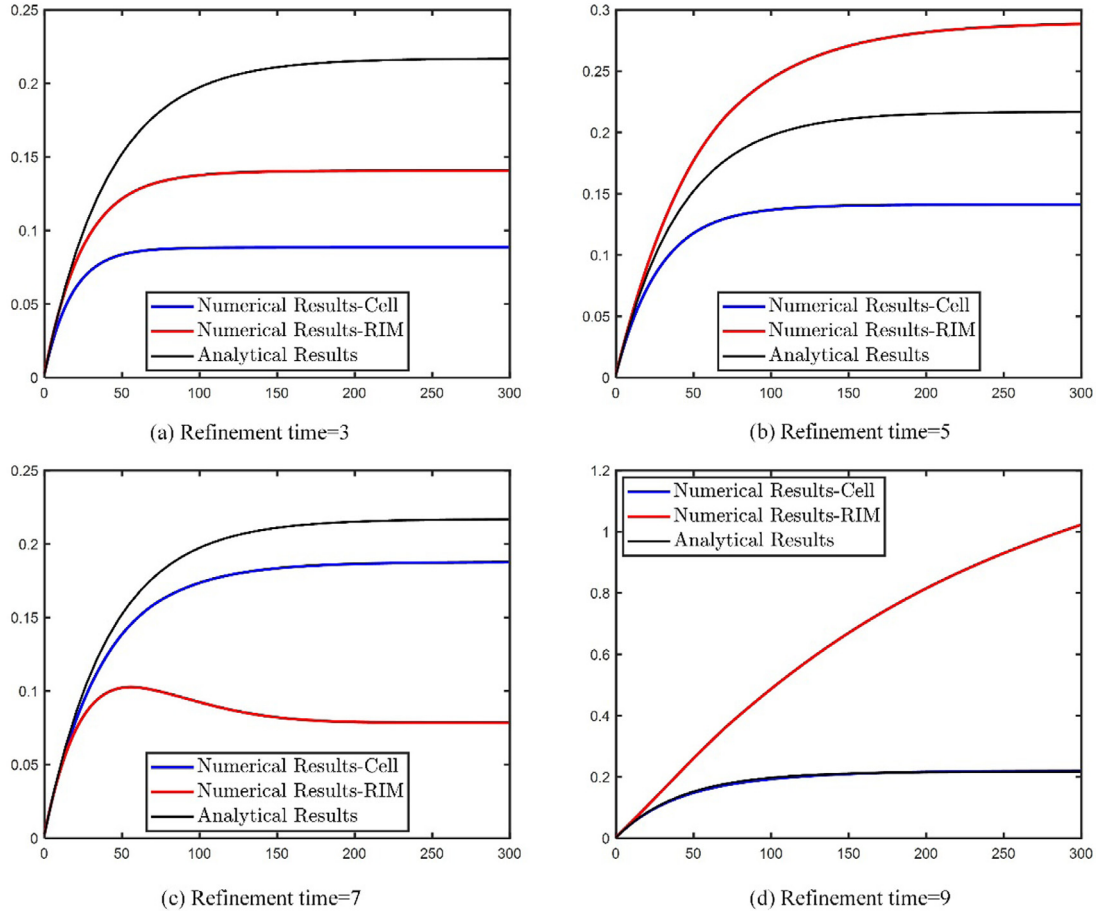


Fig. 17. The comparison between numerical results and analytical results in terms of different refinement times.

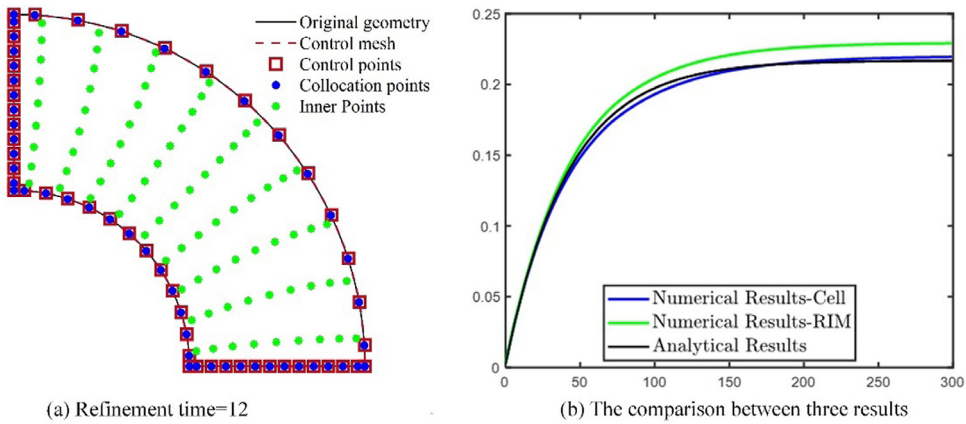


Fig. 18. The new analysis model for RIM and its numerical results.

method. The error will increase in terms of the memory stress based on the general integral relations, which means that the longer the time is, the higher the requirement of numerical accuracy will be.

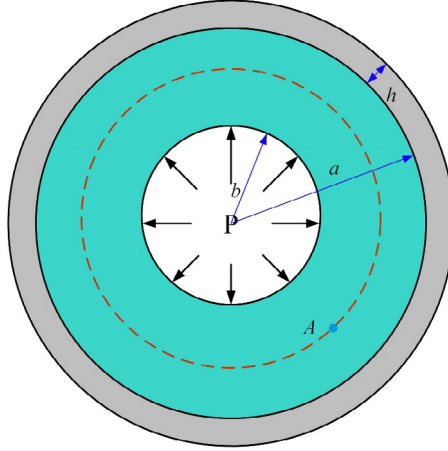


Fig. 19. Plane model for combustion chamber.

5.3. Combustion chamber of solid propellant engine

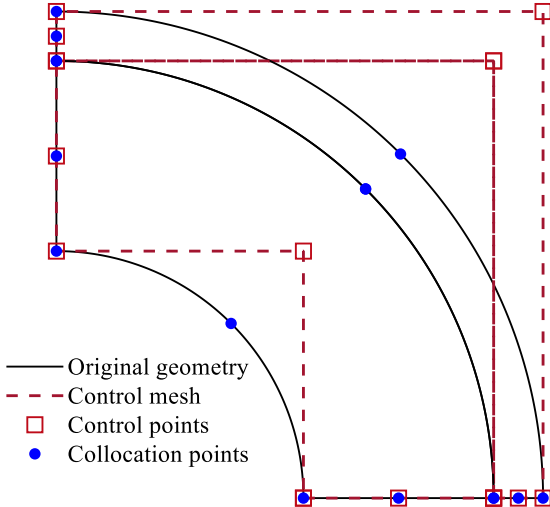
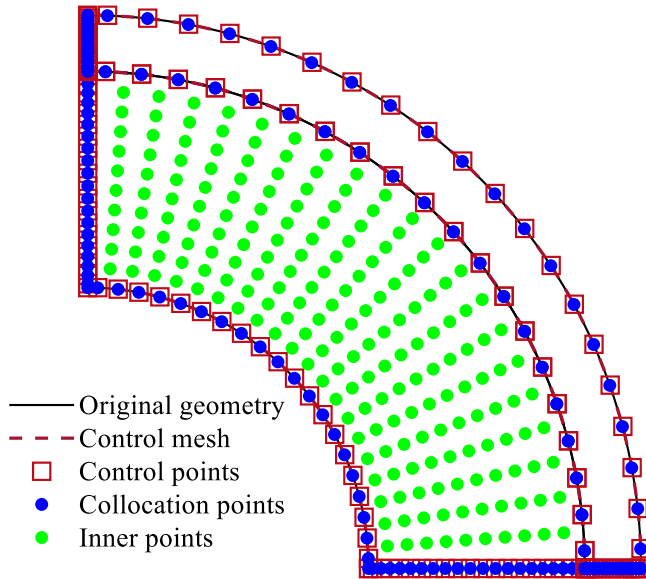
The geometric shape of combustion chamber will influence the strength and performance of solid propellant engine. Here, we consider one columnar combustion chamber of solid propellant engine and its geometry in 2D can be briefly described as Fig. 19, in which the outer ring is an elastic shell and the inner ring is a viscoelastic grain. The geometric parameters are $a = 177$, $b = 100$ and $h = 20$. The inner loading is $P(t) = p^0(1-e^{-nt}) = 6.3238(1-e^{-20t})$. And the material parameters for the elastic shell are $E_o(t) = 2E6$ and $v_o = 0.3$. The Poisson's ratio of the viscoelastic grain is $v_I = 0.45$. The relaxation elastic modulus of the viscoelastic grain can be described by Prony-series as [60]

$$E_I(t) = 7.05886 + 1.68169e^{-\frac{t}{30130.7}} + 0.98714e^{-\frac{t}{3013.07}} + 19.30384e^{-\frac{t}{301.307}} \quad (70)$$

Take the center of this viscoelastic grain as the origin of the coordinates, then the coordinate of the monitor point A is (97.9372, -97.9372). The double symmetric CAD model can be built by NURBS as shown in Fig. 20. For the analysis model in Fig. 21 200 inner points are chosen here with the same positions as shown in Fig. 12(b) to decrease the error from RIM. As shown in Fig. 22, there is an excellent consistence between numerical results and analytical results about stresses on the monitor point, which can be found in [62]. Fig. 23 shows the displacements on the monitor points in terms of time, in which radial displacements own identical tendency as shown in Fig. 6 (see Fig. 20).

5.4. Star shaped combustion chamber

Comparing with columnar combustion chamber, the star shaped combustion chamber owns bigger burning area and thrust. However, the strength of it will be damaged. Here, we consider the star shaped combustion chamber with complex geometry for grain under inner pressure as shown in Fig. 24 and its geometric parameters can be found here. The loading and material parameters are set as the same in Section 5.2 except for the Poisson's ratio $v_I = 0.48$. Ignoring the elastic part, the outer boundary condition for viscoelastic part is set as fixed boundary. Fig. 25 shows the CAD model in IGABEM. Section 5.2.2 demonstrates the effectiveness of the inner points obtained from FEM mesh in RIM. Thus, the boundary points in RIM can be obtained from CAD model after 5 h-refinements, and the inner points as shown in Fig. 26 can be obtained from the algorithm in [63]. Although the mesh in Fig. 26 is not perfect for FEM, it is sufficient for RI-IGABEM because it only needs the positions of inner points. Figs. 27 and 28 show the deformed geometries and the distribution von Mises stress of the combustion chamber at three different time points. There is no apparent difference between the results from RIM and cell discretization. Obviously, stress concentration on the groove of combustion chamber will lead to the destruction of the structure integrity of the solid propellant.

**Fig. 20.** CAD model of combustion chamber.**Fig. 21.** Analysis model of combustion chamber and the distribution of inner points.

5.5. Multiple inclusions of solid propellant

The solid propellant is usually granular composite material, in which the matrix part belongs to viscoelastic material and the inclusion part belongs to elastic material. We put the material parameters in Section 5.3 into this multi-inclusion model as shown in Fig. 29. Meanwhile, due to near incompressibility of solid propellant, the Poisson's ratio of viscoelastic matrix is set as 0.498. The geometric parameters are $h = l = 10$, and the outer loading boundary condition is the same with that in Section 5.3. The distribution of inclusions is random distribution and the volume fraction in this model is 25%. The initial geometry for CAD model can be found in Fig. 30 and the boundary points in RIM can be obtained from CAD model after 10 h -refinements. In order to avoid near singular integrals, the least distance between inner points and boundary is set as 0.12. Fig. 31 gives a part of inner points in RIM. Fig. 32 shows the deformed geometries and the distribution of von Mises stress of solid propellant at three

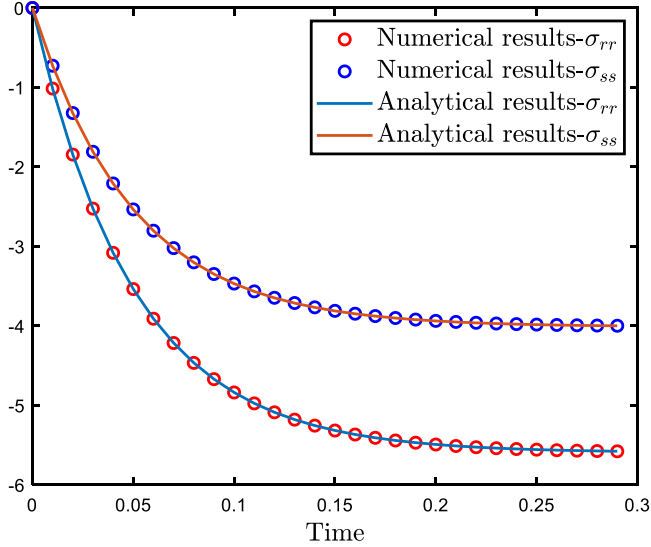


Fig. 22. Stress at the monitor point in terms of time.

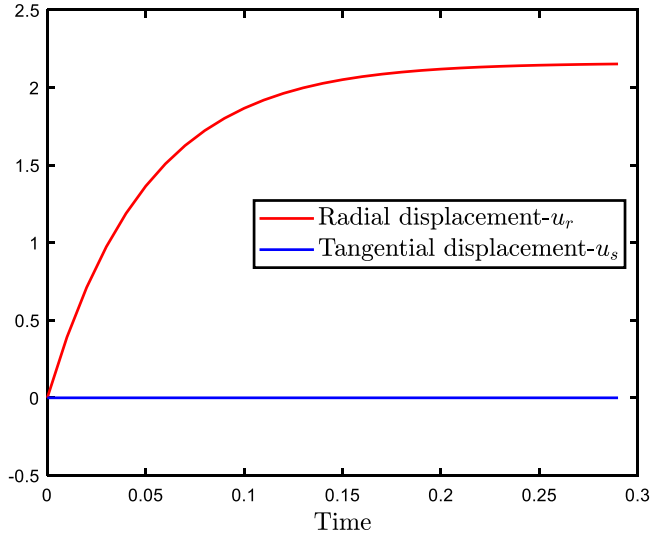


Fig. 23. Displacement on the monitor point in terms of time.

different time points. In the future work, this numerical experiment can be used to confirm the effective mechanic properties in macro mechanics, such as the generalized relaxation modulus defined by Prony series in Appendix A.

6. Conclusions

This work extended the RI-IGABEM to simulate the behaviors of viscoelastic materials: creep, relaxation and recovery. We proposed the regularized boundary-domain integral equation and its numerical implementation process. The robustness of the proposed algorithm has been verified by several numerical examples. This work can be extended into the viscoplastic analysis and related shape optimization process.

However, there are not accurate standards for the number and position of applied points in the radial integration method and the time step, which will influence the accuracy and convergence of iteration process. The nearly singular integral appears when the applied points are very close to the boundary or the thickness of the shell in Fig. 19 is very thin. These issues should be further studied in the future work.

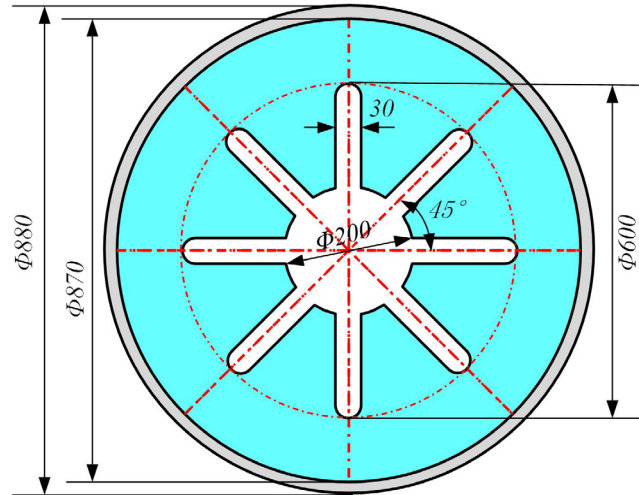


Fig. 24. Star shaped combustion chamber model.

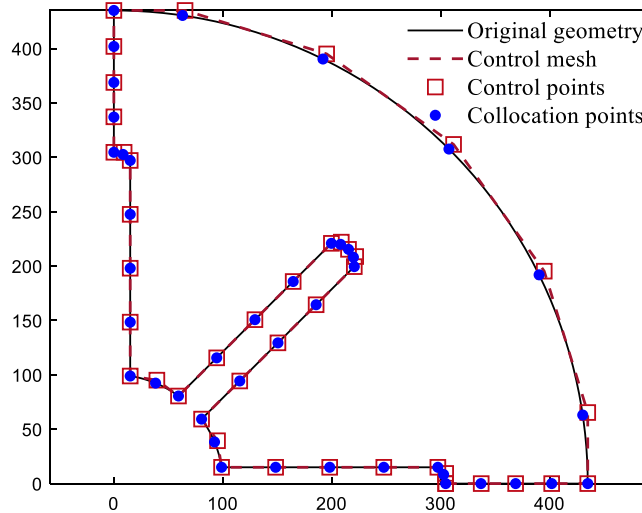


Fig. 25. CAD model for star shaped combustion chamber.

Due to the full populated matrices in BEM, the application of BEM for viscoelastic analysis of multiple inclusions will cost a lot of computer time. In the future, some accelerated algorithms such as Fast Multipole Method (FMM) [28], the wideband FMM [29], Adaptive Cross Approximation (ACA) [30], etc. must be adopted, which will be helpful for the large-scale applications of RI-IGABEM in viscoelastic problems.

Declaration of competing interest

The authors declare that they have no known competing financial interests or personal relationships that could have appeared to influence the work reported in this paper.

Acknowledgments

The research is supported by the National Natural Science Foundation of China (11972085, 11672038). Authors want to thank Dr. Quanzhang Huang of Northwestern Polytechnical University for fruitful discussions.

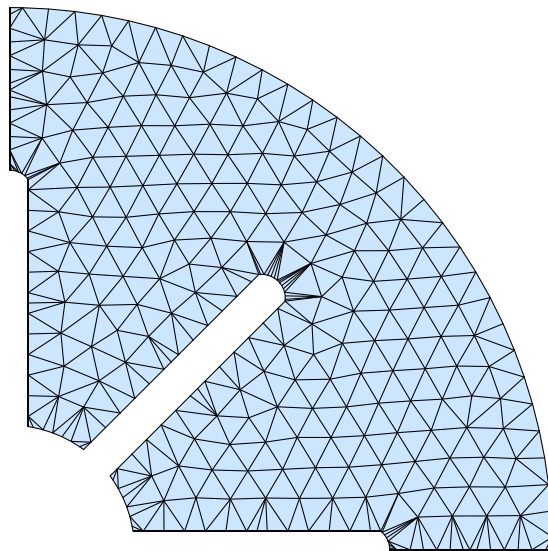


Fig. 26. The position of inner points.

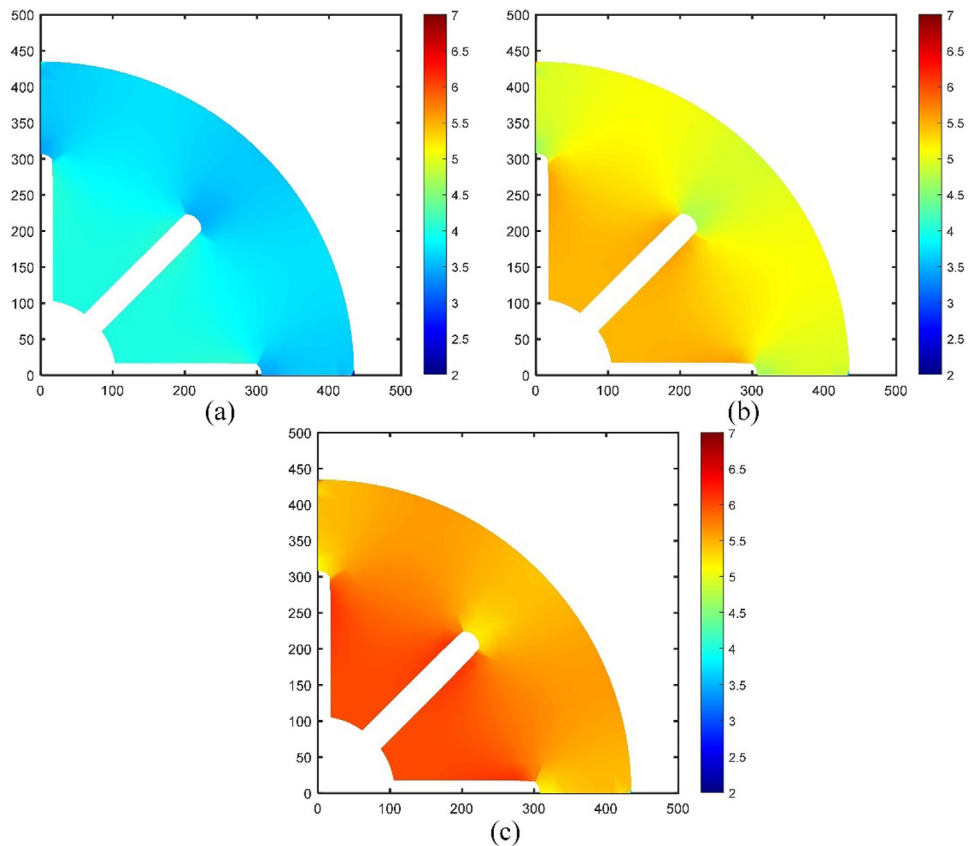


Fig. 27. The deformed geometries and the distribution of von Mises stress of the combustion chamber based on RIM: (a) $t = 0.05$; (b) $t = 0.10$; (c) $t = 0.15$.

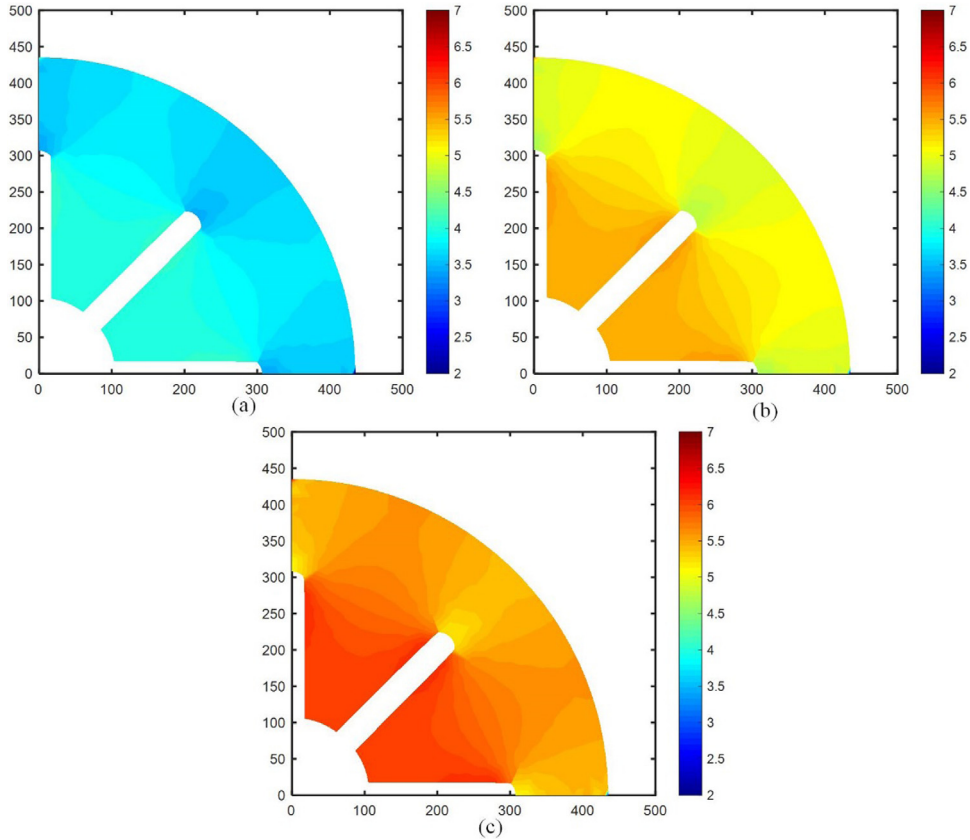


Fig. 28. The deformed geometries and the distribution of von Mises stress of the combustion chamber based on cell discretization: (a) $t = 0.05$; (b) $t = 0.10$; (c) $t = 0.15$.

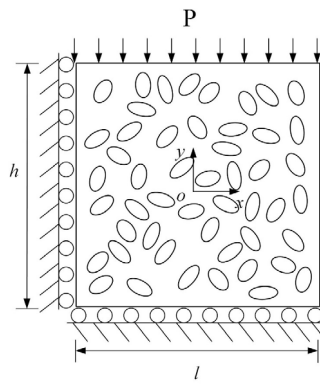


Fig. 29. Multi-inclusion model of solid propellant.

Appendix A. General integral relations

The memory stress is described by general integral relations, as shown in Eq. (30). This means we need to store all the information about strain fields in terms of coordinates and time points, which would waste too much storage

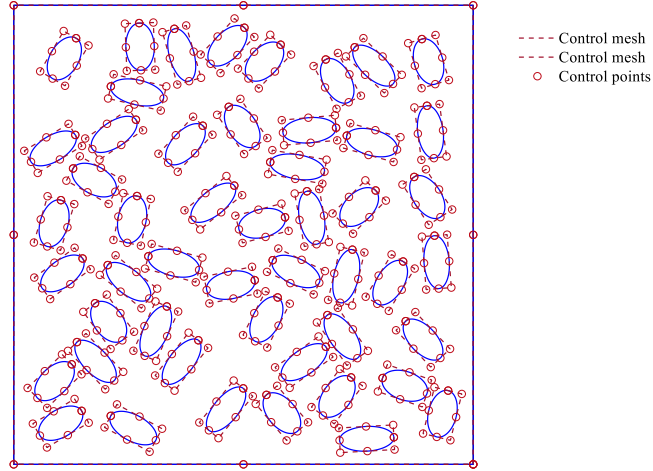


Fig. 30. CAD mode of multiple inclusion problem.

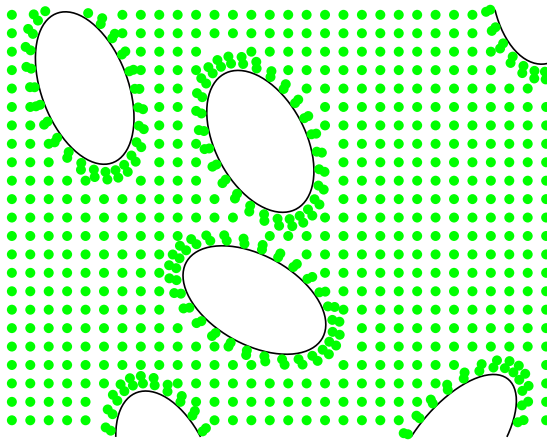


Fig. 31. The positions of inner points.

space and computational time. The first problem can be solved by RIM, in which the related variables on the applied points are only needed, and the second one can be dealt with the application of Dirichlet–Prony series to express relaxation elastic modulus, i.e.

$$G(t) = G_0 + \sum_{l=1}^m G_l \exp(-t/\tau_l) \quad (71)$$

$$K(t) = K_0 + \sum_{l=1}^m K_l \exp(-t/\zeta_l) \quad (72)$$

where τ and ζ are the relaxation times in shear and dilatational responses, respectively. In physical terms the relaxation elastic modulus corresponds to generalized Maxwell models with negative exponential functions. For many viscoelastic materials this is a good approximation for the response functions [64]. Using a trapezoidal integral and recurrence relationship can be established instead of summation. To illustrate this point, we divide the time

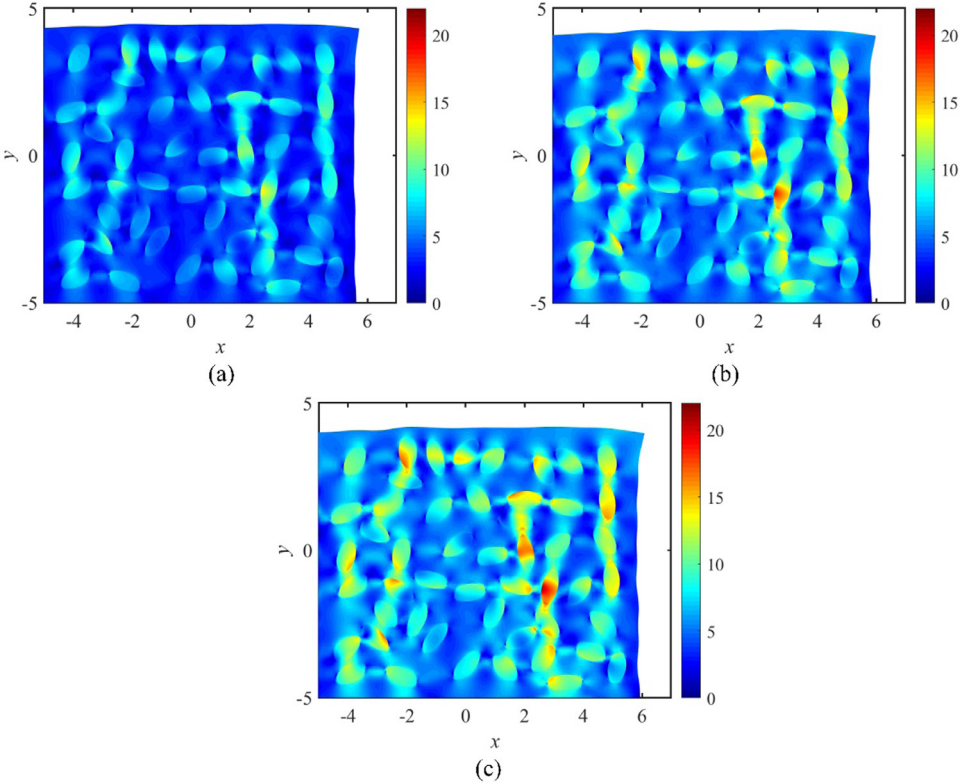


Fig. 32. Deformed geometries and von Mises stress distributions: (a) $t = 0.05$; (b) $t = 0.10$; (c) $t = 0.15$.

interval $[0, t]$ into K parts, and consider the term

$$\begin{aligned} & \int_0^{t_K} \frac{\partial G(t_K - t')}{\partial t'} \varepsilon_{ij}(\mathbf{x}, t') dt' \\ &= \frac{1}{2} \sum_{i=0}^{K-1} \sum_l^m (G_l(t_K - t_{i+1}) - G_l(t_K - t_i)) (\varepsilon_i(\mathbf{x}, t_i) + \varepsilon_{i+1}(\mathbf{x}, t_{i+1})) \\ &= \frac{1}{2} \sum_{l=1}^m (G_l(0) - G_l(t_K - t_{K-1})) (\varepsilon_K(\mathbf{x}, t_K) + \varepsilon_{K-1}(\mathbf{x}, t_{K-1})) + \frac{1}{2} \sum_{l=1}^m G_l \alpha_{l,K} \end{aligned} \quad (73)$$

in which

$$\alpha_{l,K} = \exp(-(t_K - t_{K-1})/\tau_l) [1 - \exp(-(t_{K-1} - t_{K-2})/\tau_l)] (\varepsilon_{K-1}(\mathbf{x}, t_i) + \varepsilon_{K-2}(\mathbf{x}, t_{i+1})) + \alpha_{l,K} \quad (74)$$

where the first two-time steps $\alpha_{l,1}$ and $\alpha_{l,2}$ are zero vectors. Using this recurrence relationship, only two-time step strain variables on the applied points are required. Similar recurrence expressions can be derived for the second and third integral terms in Eq. (30). Other discretion methods can be found in [60].

Appendix B. Strain on the boundary for viscoelastic problem

Considering the general integral relations in Appendix A and its application on RIM, we need to obtain the strain on the applied points including boundary points and inner points. As for the inner points, the strain can be directly acquired from Eq. (49). However, it is difficult and time-consuming to obtain the strain on the boundary points through boundary integral equations because of the corner point problem and a singular integral, thus we use a simple and efficient way combining the traction recovery method and viscoelastic constitutive formulation to derive the formulations for the boundary strain.

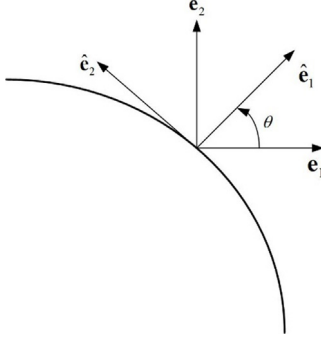


Fig. 33. Local coordinate system on curve.

The displacement gradient and the traction fields can be described as follows:

$$\begin{cases} \mathbf{u}(\xi) = \sum_{A=1}^{N_A} R_A(\xi) \tilde{\mathbf{u}}_A \\ \frac{d\mathbf{u}(\xi)}{d\xi} = \sum_{A=1}^{N_A} \frac{dR_A(\xi)}{d\xi} \tilde{\mathbf{u}}_A \\ \mathbf{t}(\xi) = \sum_{A=1}^{N_A} R_A(\xi) \tilde{\mathbf{u}}_A \end{cases} \quad (75)$$

As shown in Fig. 33, we define a local coordinate system such that \hat{e}_1 is the unit normal vector and \hat{e}_2 is the unit tangential vector as

$$\begin{cases} \hat{\mathbf{e}}_1 = \mathbf{n} \\ \hat{\mathbf{e}}_2 = \frac{\mathbf{m}}{|\mathbf{m}|} \end{cases} \quad (76)$$

where \mathbf{n} is the normal vector, and \mathbf{m} is the tangential vector in global system, and

$$\mathbf{m} = \frac{d\mathbf{x}(\xi)}{d\xi} \quad (77)$$

The transformation matrix for the quantities from the global system to the local system is

$$A = \begin{bmatrix} \hat{\mathbf{e}}_1 \\ \hat{\mathbf{e}}_2 \end{bmatrix} = \begin{bmatrix} n_1 & n_2 \\ -n_2 & n_1 \end{bmatrix} \quad (78)$$

Defining displacements, tractions, strains, and stresses in the local coordinates as \hat{u}_j , \hat{t}_j , $\hat{\epsilon}_{ij}$ and $\hat{\sigma}_{ij}$ respectively, $\hat{\epsilon}_{22}$ can be evaluated through the displacement gradient in the global coordinates,

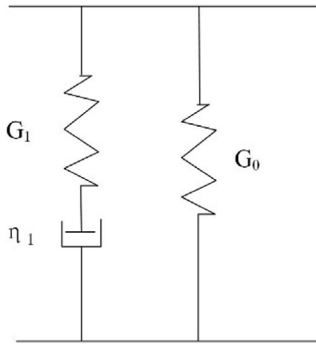
$$\hat{\epsilon}_{22}(\xi) = \hat{u}_{2,2}(\xi) = \frac{\partial \hat{u}_2}{\partial \xi} \frac{\partial \xi}{\partial \hat{x}_2} = A_{2j} \frac{\partial u_2}{\partial \xi} \frac{\partial \xi}{\partial \hat{x}_2} \quad (79)$$

The total stress tensor in the local coordinate system is

$$\begin{cases} \hat{\sigma}_{11} = \hat{t}_1 \\ \hat{\sigma}_{12} = \hat{\sigma}_{21} = \hat{t}_2 \end{cases} \quad (80)$$

As proposed in iteration process, the memory stress should be assumed before the iteration process begins at each time point. Then we can obtain the memory stress in local system as

$$\hat{\sigma}_{ij}^m = A_{ik} A_{jn} \sigma_{kn}^m \quad (81)$$

**Fig. 34.** Zener model.

According to the constitutive equations (28) and (29) of viscoelastic materials, the linear elastic stress in the local coordinate can be obtained as

$$\begin{cases} \hat{\sigma}_{11}^e = \hat{\sigma}_{11} + \hat{\sigma}_{11}^m \\ \hat{\sigma}_{12}^e = \hat{\sigma}_{12} + \hat{\sigma}_{12}^m \\ \hat{\sigma}_{22}^e = \left(\frac{E}{1-v^2}\right)\hat{\epsilon}_{22} + \left(\frac{v}{1-v}\right)\hat{\sigma}_{11}^e \end{cases} \quad (82)$$

Then the rest of total stress in the local coordinate system is

$$\hat{\sigma}_{22} = \hat{\sigma}_{22}^e - \hat{\sigma}_{22}^m \quad (83)$$

The total stress and elastic stress in the global coordinate system can be obtained as

$$\begin{cases} \sigma_{ij} = A_{ki}A_{nj}\hat{\sigma}_{kn} \\ \sigma_{ij}^e = A_{ki}A_{nj}\hat{\sigma}_{kn}^e \end{cases} \quad (84)$$

Finally, the strain in the global Cartesian coordinate system can be obtained as

$$\epsilon_{ij} = \frac{\sigma_{ij}^e}{2G} - \frac{v(1+v)}{E}\delta_{ij}\sigma_{kk}^e \quad (85)$$

Appendix C. Laplace transform solutions

In this section, correspondence principle can be used to convert elastic solutions to viscoelastic solutions by Laplace transform. Here, considering a Zener model, a simplified form of generalized Maxwell model, is shown in Fig. 34. Its relaxation modulus can be written as Prony-series as follows [60],

$$G(t) = G(0) + G_1 \exp(-t/\tau_1); \tau_1 = \eta_1/G_1 \quad (86)$$

According to correspondence principle [60], \$2G\$ and \$3K\$ can be replaced by their corresponding polynomial fractions \$\overline{Q}^G(s)/\overline{P}^G(s)\$ and \$\overline{Q}^K(s)/\overline{P}^K(s)\$, respectively. If the material is linear elastic in dilatation and viscoelastic in shear with behavior described by a Zener model, its polynomials can be written as

$$\begin{aligned} \overline{P}^K(s) &= 1, & \overline{Q}^K(s) &= 3K \\ \overline{P}^G(s) &= 1 + p_1^G s, & \overline{Q}^G &= q_0 + q_1^G s \end{aligned} \quad (87)$$

and other parameters are given as

$$p_0^G = 1; p_1^G = \tau_1; q_0^G = 2G_0; q_1^G = 2\tau_1(G_0 + G_1) \quad (88)$$

Considering plane strain state and linear elastic material, the elastic solution of displacement for simple tensile bar example as shown in Fig. 4, is given as

$$u(x) = \frac{p(1-v^2)x}{E} \quad (89)$$

Meanwhile, for the example about internal pressure into a thick-walled cylinder as shown in Fig. 10, the displacement field is found by the theory of elasticity [65] as follows

$$u = \frac{(1+v)pb^2}{E(a^2-b^2)} \left[(1-2v)r + \frac{a^2}{r} \right] \quad (90)$$

Replacing $2G$ and $3K$ by $\bar{Q}^G(s)/\bar{P}^G(s)$ and $\bar{Q}^K(s)/\bar{P}^K(s)$, the Laplace transform for the radial displacement of the related viscoelastic problem is obtained as follows

$$\bar{u} = \frac{\bar{p}b^2}{(a^2-b^2)} \frac{\bar{P}^G}{\bar{Q}^G} \left(\frac{3\bar{P}^K\bar{Q}^G}{2\bar{P}^G\bar{Q}^K + \bar{P}^K\bar{Q}^G} r + \frac{a^2}{r} \right) \quad (91)$$

Assuming $p(t) = pH(t)$, its Laplace transform is $\bar{p}(s) = \frac{p}{s}$. Substituting the polynomials (87) into (91), we obtain

$$\bar{u} = \frac{pb^2}{(a^2-b^2)} \left\{ \frac{3(1+p_1^Gs)r}{s[6K+q_0^G+(6Kp_1^G+q_1^Gs)s]} + \frac{a^2}{r} \frac{1+p_1^Gs}{s(q_0^G+q_1^Gs)} \right\} \quad (92)$$

Through the symbolic function *ilaplace* in Matlab, the displacement solution for viscoelastic problem can be obtained as

$$u = \text{ilaplace}(\bar{u}) \quad (93)$$

The analytical solution for the simple tensile bar can be acquired through the same procedures in Eqs. (90)–(93). Step and impulse functions are used here:

References

- [1] L.F. Simões Hoffmann, F.C. Parquet Bizarria, J.W. Parquet Bizarria, Detection of liner surface defects in solid rocket motors using multilayer perceptron neural networks, *Polym. Test.* 88 (2020) 106559.
- [2] R. Marimuthu, B. Nageswara Rao, Development of efficient finite elements for structural integrity analysis of solid rocket motor propellant grains, *Int. J. Press. Vessels Pip.* 111–112 (2013) 131–145.
- [3] O.C. Zienkiewicz, R.L. Taylor, J.Z. Zhu, *The Standard Discrete System and Origins of the Finite Element Method*, Butterworth-Heinemann, Oxford, 2013.
- [4] T.A. Cruse, A direct formulation and numerical solution of the general transient elastodynamic problem. II, *J. Math. Anal. Appl.* 22 (1968) 341–355.
- [5] T.A. Cruse, Numerical solutions in three dimensional elastostatics, *Int. J. Solids Struct.* 5 (1969) 1259–1274.
- [6] J.A. Cottrell, T.J.R. Hughes, Y. Bazilevs, *Isogeometric Analysis: Toward Integration of CAD and FEA*, Wiley, UK, 2009.
- [7] B. Marussig, J. Zechner, G. Beer, T.-P. Fries, Fast isogeometric boundary element method based on independent field approximation, *Comput. Methods Appl. Mech. Engrg.* 284 (2015) 458–488.
- [8] G. Beer, B. Marussig, C. Duenser, *The Isogeometric Boundary Element Method*, Springer, 2020.
- [9] G. Beer, C. Duenser, Isogeometric boundary element analysis of problems in potential flow, *Comput. Methods Appl. Mech. Engrg.* 347 (2019) 517–532.
- [10] J. Gu, J. Zhang, G. Li, Isogeometric analysis in BIE for 3-D potential problem, *Eng. Anal. Bound. Elem.* 36 (2012) 858–865.
- [11] H. Lian, P. Kerfriden, S.P.A. Bordas, Implementation of regularized isogeometric boundary element methods for gradient-based shape optimization in two-dimensional linear elasticity, *Internat. J. Numer. Methods Engrg.* 106 (2016) 972–1017.
- [12] C. Liu, L.L. Chen, W.C. Zhao, H.B. Chen, Shape optimization of sound barrier using an isogeometric fast multipole boundary element method in two dimensions, *Eng. Anal. Bound. Elem.* 85 (2017) 142–157.
- [13] L.L. Chen, H. Lian, Z. Liu, H.B. Chen, E. Atroshchenko, S.P.A. Bordas, Structural shape optimization of three dimensional acoustic problems with isogeometric boundary element methods, *Comput. Methods Appl. Mech. Engrg.* 355 (2019) 926–951.
- [14] C. Xu, C. Dong, R. Dai, RI-IGABEM based on PIM in transient heat conduction problems of FGMs, *Comput. Methods Appl. Mech. Engrg.* 374 (2021) 113601.
- [15] X. Peng, E. Atroshchenko, P. Kerfriden, S.P.A. Bordas, Isogeometric boundary element methods for three dimensional static fracture and fatigue crack growth, *Comput. Methods Appl. Mech. Engrg.* 316 (2017) 151–185.
- [16] M.J. Peake, J. Trevelyan, G. Coates, Extended isogeometric boundary element method (XIBEM) for two-dimensional Helmholtz problems, *Comput. Methods Appl. Mech. Engrg.* 259 (2013) 93–102.
- [17] M. Yoon, J. Lee, B. Koo, Shape design optimization of thermoelasticity problems using isogeometric boundary element method, *Adv. Eng. Softw.* 149 (2020) 102871.
- [18] D. Sun, C. Dong, Shape optimization of heterogeneous materials based on isogeometric boundary element method, *Comput. Methods Appl. Mech. Engrg.* 370 (2020) 113279.
- [19] Q. Hu, F. Chouly, P. Hu, G. Cheng, S.P.A. Bordas, Skew-symmetric Nitsche's formulation in isogeometric analysis: Dirichlet and symmetry conditions, patch coupling and frictionless contact, *Comput. Methods Appl. Mech. Engrg.* 341 (2018) 188–220.

- [20] V.P. Nguyen, P. Kerfriden, M. Brino, S.P.A. Bordas, E. Bonisoli, Nitsche's method for two and three dimensional NURBS patch coupling, *Comput. Mech.* 53 (2014) 1163–1182.
- [21] M.J. Peake, J. Trevelyan, G. Coates, Extended isogeometric boundary element method (XIBEM) for three-dimensional medium-wave acoustic scattering problems, *Comput. Methods Appl. Mech. Engrg.* 284 (2015) 762–780.
- [22] K.V. Kostas, A.I. Ginnis, C.G. Politis, P.D. Kaklis, Ship-hull shape optimization with a T-spline based BEM-isogeometric solver, *Comput. Methods Appl. Mech. Engrg.* 284 (2015) 611–622.
- [23] L. Coox, F. Greco, O. Atak, D. Vandepitte, W. Desmet, A robust patch coupling method for NURBS-based isogeometric analysis of non-conforming multipatch surfaces, *Comput. Methods Appl. Mech. Engrg.* 316 (2017) 235–260.
- [24] A.I. Ginnis, K.V. Kostas, C.G. Politis, P.D. Kaklis, K.A. Belibassakis, T.P. Gerochristis, M.A. Scott, T.J.R. Hughes, Isogeometric boundary-element analysis for the wave-resistance problem using T-splines, *Comput. Methods Appl. Mech. Engrg.* 279 (2014) 425–439.
- [25] Y.J. Wang, D.J. Benson, A.P. Nagy, A multi-patch nonsingular isogeometric boundary element method using trimmed elements, *Comput. Mech.* 56 (2015) 173–191.
- [26] V.P. Nguyen, C. Anitescu, S.P.A. Bordas, T. Rabczuk, Isogeometric analysis: An overview and computer implementation aspects, *Math. Comput. Simulation* 117 (2015) 89–116.
- [27] A. Yadav, R.K. Godara, G. Bhardwaj, A review on XIGA method for computational fracture mechanics applications, *Eng. Fract. Mech.* 230 (2020) 107001.
- [28] L. Greengard, V. Rokhlin, A fast algorithm for particle simulations, *J. Comput. Phys.* 73 (1987) 325–348.
- [29] C.J. Zheng, C.X. Bi, C.Z. Zhang, Y.B. Zhang, H.B. Chen, Fictitious eigenfrequencies in the BEM for interior acoustic problems, *Eng. Anal. Bound. Elem.* 104 (2019) 170–182.
- [30] M. Bebendorf, Approximation of boundary element matrices, *Numer. Math.* 86 (2000) 565–589.
- [31] G. Beylkin, R. Coifman, V. Rokhlin, Fast wavelet transforms and numerical algorithms I, *Commun. Pure Appl. Math. Comput.* 44 (2010) 141–183.
- [32] J.R. Phillips, J.K. White, A Precorrected-FFT method for electrostatic analysis of complicated 3-d structures, *IEEE Trans. Comput.-Aided Des. Integr. Circuits Syst.* 16 (1997) 1059–1072.
- [33] A. Lorenzana, J.A. Garrido, Analysis of the elastic–plastic problem involving finite plastic strain using the boundary element method, *Comput. Struct.* 73 (1999) 147–159.
- [34] H. Gun, Elasto-plastic static stress analysis of 3D contact problems with friction by using the boundary element method, *Eng. Anal. Bound. Elem.* 28 (2004) 779–790.
- [35] C.Y. Dong, Z.H. Yao, Q.H. Du, Application of boundary element method in 2-D elasto-plastic contact problem, in: W.B. Lee (Ed.), *Advances in Engineering Plasticity and Its Applications*, Elsevier, Oxford, 1993, pp. 653–658.
- [36] X.-W. Gao, B.-J. Zheng, K. Yang, C. Zhang, Radial integration BEM for dynamic coupled thermoelastic analysis under thermal shock loading, *Comput. Struct.* 158 (2015) 140–147.
- [37] J.C.F. Telles, A self-adaptive co-ordinate transformation for efficient numerical evaluation of general boundary element integrals, *Internat. J. Numer. Methods Engrg.* 24 (1987) 959–973.
- [38] H.B. Chen, P. Lu, M.G. Huang, F.W. Williams, An effective method for finding values on and near boundaries in the elastic BEM, *Comput. Struct.* 69 (1998) 421–431.
- [39] Y. Liu, T.J. Rudolphi, Some identities for fundamental solutions and their applications to weakly-singular boundary element formulations, *Eng. Anal. Bound. Elem.* 8 (1991) 301–311.
- [40] Y.J. Liu, T.J. Rudolphi, New identities for fundamental solutions and their applications to non-singular boundary element formulations, *Comput. Mech.* 24 (1999) 286–292.
- [41] Y.J. Liu, On the simple-solution method and non-singular nature of the BIE/BEM — a review and some new results, *Eng. Anal. Bound. Elem.* 24 (2000) 789–795.
- [42] L. Ma, A.M. Korsunsky, A note on the Gauss-Jacobi quadrature formulae for singular integral equations of the second kind, *Int. J. Fract.* 126 (2004) 399–405.
- [43] O. Huber, A. Lang, G. Kuhn, Evaluation of the stress tensor in 3D elastostatics by direct solving of hypersingular integrals, *Internat. J. Numer. Methods Engrg.* 39 (1993) 2555–2573.
- [44] G. Karami, D. Derakhshan, An efficient method to evaluate hypersingular and supersingular integrals in boundary integral equations analysis, *Eng. Anal. Bound. Elem.* 23 (1999) 317–326.
- [45] M. Cerrolaza, E. Alarcon, A bi-cubic transformation for the numerical evaluation of the Cauchy principal value integrals in boundary methods, *Internat. J. Numer. Methods Engrg.* 28 (1989) 987–999.
- [46] Z. Niu, X. Wang, H. Zhou, Non-singular algorithm for the evaluation of the nearly singular integrals in boundary element methods, *Chinese J. Appl. Mech.* 18 (2001) 1–8.
- [47] H.R. Kutt, The numerical evaluation of principal value integrals by finite-part integration, *Numer. Math.* 24 (1975) 205–210.
- [48] X.W. Gao, An effective method for numerical evaluation of general 2D and 3D high order singular boundary integrals, *Comput. Methods Appl. Mech. Engrg.* 199 (2010) 2856–2864.
- [49] Y.P. Gong, C.Y. Dong, X.C. Qin, An isogeometric boundary element method for three dimensional potential problems, *J. Comput. Appl. Math.* 313 (2017) 454–468.
- [50] R.N. Simpson, S.P.A. Bordas, J. Trevelyan, T. Rabczuk, A two-dimensional isogeometric boundary element method for elastostatic analysis, *Comput. Methods Appl. Mech. Engrg.* 209–212 (2012) 87–100.
- [51] G. Beer, B. Marussig, J. Zechner, C. Dünser, T.-P. Fries, Isogeometric boundary element analysis with elasto-plastic inclusions. Part 1: Plane problems, *Comput. Methods Appl. Mech. Engrg.* 308 (2016) 552–570.
- [52] G. Beer, V. Mallardo, E. Ruocco, B. Marussig, J. Zechner, C. Dünser, T.-P. Fries, Isogeometric boundary element analysis with elasto-plastic inclusions. Part 2: 3-D problems, *Comput. Methods Appl. Mech. Engrg.* 315 (2017) 418–433.

- [53] Y.C. Fung, D. Drucker, Foundation of Solid Mechanics, Prentice-Hall, New Jersey, 1965.
- [54] E.H. Lee, Stress analysis for linear viscoelastic materials, *Rheol. Acta* 1 (1961) 426–430.
- [55] M.L. Williams, R.F. Landel, J.D. Ferry, The temperature dependence of relaxation mechanisms in amorphous polymers and other glass-forming liquids, *J. Am. Chem. Soc.* 77 (1955) 3701–3707.
- [56] Q. Huang, J. Chen, H. Qiang, X. Wang, C. Yue, A. Li, Boundary element method for local stress field analysis of inclusions in solid propellant grain, *J. Soild Rocket Technol.* 42 (2019) 275–307.
- [57] Y.P. Gong, H.S. Yang, C.Y. Dong, A novel interface integral formulation for 3D steady state thermal conduction problem for a medium with non-homogenous inclusions, *Comput. Mech.* 63 (2019) 181–199.
- [58] P.K. Banerjee, S.T. Raveendra, Advcanced boundary element analysis of two- and three-dimensional problems of elasto-plasticity, *Intern. J. Numer. Methods Eng.* 23 (1986) 985–1002.
- [59] W.Z. Feng, L.-F. Gao, J.-M. Du, W. Qian, X.-W. Gao, A meshless interface integral BEM for solving heat conduction in multi-non-homogeneous media with multiple heat sources, *Int. Commun. Heat Mass Transfer* 104 (2019) 70–82.
- [60] S.P.C. Marques, G.J. Creus, Computational Viscoelasticity, London, 2012.
- [61] Y.J. Wang, D.J. Benson, Multi-patch nonsingular isogeometric boundary element analysis in 3D, *Comput. Methods Appl. Mech. Engrg.* 293 (2015) 71–91.
- [62] E.C. Ting, Stress analysis for linear viscoelastic cylinders, 8 (1970) 18–22.
- [63] P.-O. Persson, G. Strang, A simple mesh generator in MATLAB, 46 (2004) 329–345.
- [64] R.L. Taylor, K.S. Pister, G.L. Goudreau, Thermomechanical analysis of viscoelastic solids, 2 (1970) 45–59.
- [65] J. Altenbach, Z. Mechanic, Book review: Martin H. Sadd Elasticity – Theory, applications, and numerics, *J. Appl. Math.* 85 (2010) 907–908.